Journal of Materials Science & Technology 160 (2023) 161–180

Contents lists available at ScienceDirect

Journal of Materials Science & Technology

journal homepage: www.elsevier.com/locate/jmst

Review Article

Design of high-performance molybdenum alloys via doping metal oxide and carbide strengthening: A review

Hairui Xing[a,b], Ping Hu[a,b,*], Chaojun He[a,b], Xiangyang Zhang[a,b], Jiayu Han[a,b], Fan Yang[a,b], Run Bai[a,c], Wen Zhang[c,**], Kuaishe Wang[a,b], Alex A. Volinsky[d]

[a] School of Metallurgy Engineering, Xi'an University of Architecture and Technology, Xi'an 710055, China
[b] National and Local Joint Engineering Research Center for Functional Materials Processing, Xi'an University of Architecture and Technology, Xi'an 710055, China
[c] Northwest Institute for Non-ferrous Metal Research, Xi'an 710016, China
[d] Department of Mechanical Engineering, University of South Florida, 4202 E. Fowler Ave. ENG 030, Tampa, FL 33620, USA

ARTICLE INFO

Article history:
Received 16 January 2023
Revised 13 March 2023
Accepted 27 March 2023
Available online 24 April 2023

Keywords:
Molybdenum alloy
Metal oxide and carbide addition
Oxide dispersion-strengthened
Carbide precipitation-strengthened
Microstructure
Mechanical properties

ABSTRACT

Metal oxide and carbide strengthening molybdenum (Mo) alloys have been designed as promising advanced materials in refractory metals to solve some of the core engineering problems in superalloy applications. Hence, there is a need to summarize the results obtained and evaluate the opportunities for preparing high-performance Mo alloys by strengthening metal oxides and carbides to improve the performance characteristics of Mo metal materials. This paper reviews the results of the reported work concerning the structure and properties of Mo alloys with different metal oxide and carbide strengthening methods added to Mo matrix. The influence of the doping of La_2O_3 and Y_2O_3 particles, ceramic Al_2O_3 and ZrO_2 particles, and refractory TiC and ZrC carbides particles of Mo alloys are discussed. The impacts of particle morphology, size, distribution and volume fractions of oxide and carbide are analyzed, as well as the specific features of different doping techniques for obtaining high-performance Mo alloys materials. This work will guide future research on the design of high-performance refractory Mo alloys by adding oxides and carbide particles, helping to solve the core issues in the field of superalloy application research.

1. Introduction

Molybdenum (Mo) and Mo alloys have a series of excellent physical and chemical properties, including a high melting point of 2620 °C, good high-temperature strength, corrosion resistance, and thermal conductivity [1–3]. They have been widely used as high-temperature resistant structural materials in aerospace engineering [4–6], electronics [7,8], nuclear fusion reactors [9], metal processing [10–12], medical equipment, and other fields [13–15]. However, the recrystallization temperature, strength and hardness at high temperatures of Mo alloys cannot be met the increasing requirements of scientific and technological development [16,17]. Therefore, the design of high-temperature-resistant Mo alloys with high strength and toughness has become a research hotspot [18–20]. Since Mo has the intrinsic characteristics of electronic structure in body-centered cubic (bcc) metals [21], especially the non-extrinsic brittleness is caused by the segregation of interstitial atoms such as oxygen and nitrogen at grain boundaries (GBs) [22,23]. It not only causes issues of low-temperature brittleness and insufficient high-temperature oxidation resistance but also leads to difficulties in deep processing of Mo [24,25], limiting its wide application as high-temperature structural materials [26,27]. To improve the strength and reduce the brittleness of Mo alloys, their comprehensive properties can be controlled by adding Re and W alloying elements [28], along with doping Al, K, and Si [29], and oxide/carbides strengthening.

An effective way to improve the high temperature strength, low temperature plasticity, and oxidation resistance of Mo is alloying design [30–32]. The binary or multi-system Mo alloys with good all-round properties have been prepared by solid solution strengthening and dispersion strengthening with alloying design using trace or massive elements [33–35]. Dispersion strengthening is one of the alloying design methods to promote the performance of Mo matrices [36]. If the compound is in the form of dispersed particles or granules in the grains of the solid solution, the

* Corresponding author at: School of Metallurgy Engineering, Xi'an University of Architecture and Technology, Xi'an 710055, China.
** Corresponding author.
E-mail addresses: huping@xauat.edu.cn (P. Hu), gwenzh@163.com (W. Zhang).

https://doi.org/10.1016/j.jmst.2023.03.026
1005-0302/

strength and hardness of the alloy can be improved significantly with only a slight decrease in plasticity and toughness. The finer evenly distributed particles result in a better strengthening effect [37]. Adding stable metal oxides and carbides to molybdenum can form a new type of strengthened Mo alloy. Alloys produced by powder metallurgy (PM) are considered dispersion-strengthened alloys [38]. For dispersion-strengthened particles, dislocations can only bypass these large particles by a bypass mechanism due to the direct incorporation of stable, high melting point particles by mechanical alloying or other advanced mixing techniques, where particle sizes may reach around 1 μm. According to the Orovan's description of dislocation-particle interactions, the moving dislocation will be subjected to great resistance, forcing the stress to increase in the process of continuous deformation to overcome the reverse stress. The larger number of particles results in smaller spacing between them with a more obvious strengthening effect according to the dislocation theory. The uniformly dispersed particles can pin dislocations and GBs, refine grains, and strengthen the Mo alloy matrix. The Mo alloy strength can be improved by refining particles, reducing their size, or increasing volume fraction. Currently, oxides and carbides are the main strengthening phases. These oxides are rare earth oxides (La_2O_3 [39], Y_2O_3 [40] and CeO_2 [41]), metal ceramic oxides (Al_2O_3 [42–44] and ZrO_2 [45]) and carbides mainly include TiC [46], ZrC [47] and HfC [48].

Metal oxides and carbides strengthening Mo alloys have broad development prospects [49]. Oxides reinforcements are favored [50] because of high-temperature stability and low prices, such as rare earth lanthanum and yttrium oxides for Mo doping. Dispersed ultrafine La_2O_3 particles can effectively refine Mo microstructure and improve the mechanical properties of Mo alloys [51,52]. Oxide-dispersed particles can also accelerate the sintering process of Mo alloys. Carbides have excellent mechanical properties, high hardness, melting point, and good thermal stability, and have important applications in composite materials. Mo alloys reinforced with TiC and ZrC particles have refined grains and excellent thermal stability.

The present paper aims to summarize the effects of oxide and carbide addition on the microstructure and mechanical properties of Mo alloys. The relationships between the microstructure and properties of Mo alloys for each metal oxide/carbide are discussed. First, we introduce the oxide strengthening design and carbide strengthening design, Next, some recent examples involving different oxide and carbide powder addition, the impacts of particle morphology, size, distribution, and volume fractions of oxide and carbide are analyzed, as well as the specific features of different doping techniques for obtaining high-performance Mo alloys materials. Finally, we discuss the current challenges and opportunities of high-performance Mo alloys, which have great potential as materials for industrial applications and production based on metal oxides and carbides strengthening. It is hoped that this work can act as a guide for future researchers on topics that contribute to the development of superalloy application.

2. Oxide dispersion-strengthened design

Metal oxides are often used as reinforcements to improve the strength and toughness of Mo alloys. Adding oxide dispersion strengthening is a method in which oxide particles are dispersed in the alloy matrix as hard particles. It refers to the strengthening of ultrafine high-melting point oxides insoluble in the metal matrix as the secondary phase. Metal oxide reinforced Mo metals are typically prepared by PM to promote uniform distribution of the particles in the base metal. The addition of metal oxides not only increases the recrystallization temperature of the Mo alloys and improves their sag resistance, but also improves high-temperature creep properties. La, Ce, Al, and Zr are commonly used for the dispersion strengthening of Mo alloys with oxides formed by rare earth elements. Depending on the doped metal oxides, they are broadly classified as rare earth element oxides doped with La_2O_3 and Y_2O_3, and ceramic Al_2O_3 and ZrO_2. The techniques for preparing high-strength and tough Mo-doped alloys include mechanical alloying, pressurelesps sintering, hot isostatic pressing, and plasma sintering, etc. The research focus is mainly on the synthesis of ultrafine oxide powders with high sintering activity [53], along with the strengthening and toughening mechanisms of Mo alloys doped with oxides.

2.1. Doped with La_2O_3 particles

The development of rare earth La_2O_3 oxide-dispersed Mo alloys have been ongoing, as high melting point La_2O_3 can effectively improve the recrystallization temperature and microstructure stability of Mo alloys [39,54]. The La_2O_3 particle doping has a significant influence on the alloy microstructure, morphology, mechanical properties, high-temperature mechanical properties, and chemical properties of Mo alloys [39,55,56]. The diffuse distribution of fine La_2O_3 particles in the Mo matrix improves the strength and toughness of Mo alloy. Many studies have reported in [57–60] that different doping methods will also change the effect of La_2O_3 particles, improving the properties of Mo alloys. This section explores the La_2O_3 particles addition on the particle morphology of Mo powder and the effect on the grain size of Mo alloys. The effective doping methods of La_2O_3 particles and the influence of particle dispersion on the mechanical properties of the Mo matrix at room temperature and high temperature are obtained.

Due to the high surface activity of rare earth elements [61], the particle morphology of Mo powder is affected by La_2O_3 particles. Sun et al. [62] used a facile hydrothermal synthesis of oxide-doped Mo powders and found that doping La_2O_3 particles could affect the crystallinity and particle size of MoO_3 powders. For La_2O_3 particles, La^{3+} and Mo^{4+} have a strong interaction (Fig. 1), which changed the coordination of Mo and O, forming MoO_2 in a polygonal state. These three oxides had similar effects of inhibiting grain growth and promoting grain refinement, while La_2O_3 changed the growth morphology of Mo particles.

Except for the hydrothermal synthesis, the solid-liquid doping and liquid-liquid doping methods can effectively control the grain size and comprehensive properties of Mo alloys [63]. The La_2O_3 solid-state doping method and hot-pressing sintering technology cause grain refinement with an average grain size of 2.7 mm, resulting in the highest yield strength of the Mo-La_2O_3 alloy [51]. Freeze drying has been proposed as a promising technology for nanocrystals, nano oxide particles, and high-density oxide dispersion-strengthened (ODS) Mo alloys. It provides an excellent solution for the ultrafine size and high sintering activity of Mo-La_2O_3 composite powder. Hu et al. [64] fabricated Mo-La_2O_3 composite nano-powders with high sintering activity by the freeze-drying method. The Mo-La_2O_3 alloy had a high 98.1% relative density after sintering at 1500 °C. The results indicate that the Mo alloy sintered at low temperature has fine oxide particles (< 5 nm), high hardness (495 $HV_{0.2}$), and strength (1201 MPa) at 30% strain compared with the related ODS-Mo alloy. The grain size of Mo-$La_xMo_yO_z$ alloy is 440 nm, which is much smaller than the traditional ODS Mo (3–60 μm) reported in tRefs. [65–67]. It has been demonstrated in Ref. [68] that a hierarchical microstructure in La_2O_3 nanoparticles-doped Mo alloy is successfully designed and manufactured by the liquid-liquid mixing process, which can control the uniform distribution of grain size and nano-sized particles in the nanostructure region.

However, the reason for the effective grain size refinement of Mo alloys by rare earth La_2O_3 is that the particles can effectively

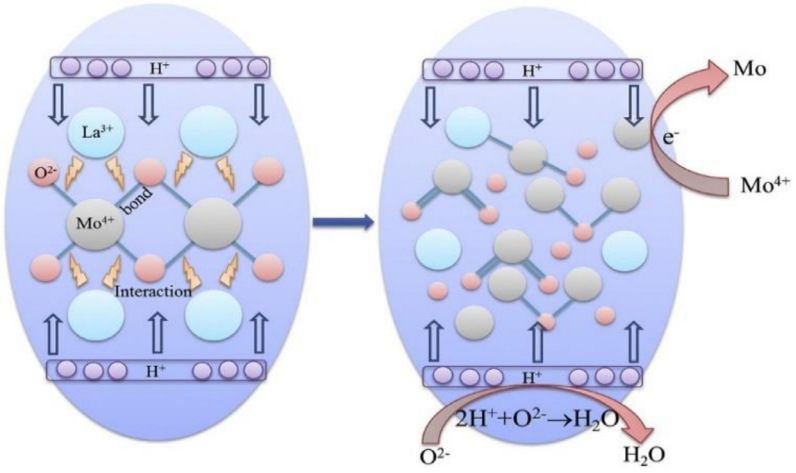

Fig. 1. Schematic illustration of the nucleation step involved in the interaction of La^{3+} and Mo^{4+}. Adapted with permission from Ref. [62]. Reprinted from International Journal of Refractory Metals and Hard Materials, 5396390978725, Copyright (2022), with permission from Elsevier.

hinder the movement of GBs, thereby improving the properties of Mo alloys [69–71]. Jiang et al. [72] doped La_2O_3 and CeO_2 particles in the Mo-Y_2O_3 alloy by wet chemical method and low-temperature sintering. They explored the reasons for the grain refinement mechanism by La_2O_3 doping. For the Mo alloys, the two key steps that ultimately determine the microstructure were the reduction and sintering processes. The effects of uniformly distributed oxides on GB inhibit grain growth during sintering. The oxide particles on GBs migration were analyzed using theoretical calculations and calculated two pinning forces, including the Zener force and interfacial resistance caused by changes in interfacial free energy. The quantitative calculation of the Zener force is as follows [69]:

$$Z_P = 3\gamma_{GB}F_v/(2r) \tag{1}$$

Here, γ_{GB} is the GBs energy of the secondary phase, F_v is the volume fraction of oxide particles, and r represents the average radius of oxide particles. According to Eq. (1), the Zener forces of Mo-Y, Mo-Y-La, and Mo-Y-Ce alloys are calculated to be 4.68×10^{-2} MPa, 7.76×10^{-2} MPa, and 4.33×10^{-2} MPa, respectively, indicating that La_2O_3 doping has a strong effect of pinning Mo-Y alloys. On the other hand, the effects of different dopants on the interfacial resistance of Mo alloys are calculated. The interfacial energy change is given as [73]:

$$\Delta C = 4\pi r^2(\gamma_2 - \gamma_1) \tag{2}$$

Then the interface resistance is

$$F = 8\pi r(\gamma_2 - \gamma_1) \tag{3}$$

Here, r is the radius of spherical particles; γ_1 and γ_2 is the interfacial free energy of particles in growing and vanishing grains, respectively. Different interfacial resistance is analyzed through the process of different dopants affecting the diffusion in Mo alloy. It can be speculated that compared with other oxide particles, Mo atoms can significantly diffuse into the oxide particles of the Mo-Y-La alloy, which further indicates that the La element can attract or bind Mo atoms, reduce the interface free energy, and increase the interface resistance. Consequently, the rhenium oxide particles at the GBs can effectively improve the Zener force and interfacial resistance, which eventually leads to the migration of GBs and inhibits the grain growth of the Mo alloy, resulting in the Mo-Y_2O_3 alloy having excellent strength and hardness. This also provides theoretical guidance for the selection of suitable oxide dopants for the preparation of ODS alloys with excellent mechanical properties.

The La_2O_3 particles can be successfully dispersed in the Mo alloy [74], improving its room temperature mechanical properties [75–85]. Lin et al. [86] studied the effects of La_2O_3 on the room temperature mechanical properties of Mo-12Si-8.5B alloy by adding La_2O_3 particles with different contents (0–0.9 wt.%). It is indicated that the different La_2O_3 can improve the room compression strength and fracture toughness of Mo-12Si-8.5B alloy. When the content of La_2O_3 is 0.9 wt.%, Mo-12Si-8.5B alloy has better room temperature compressive strength and yield strength (2806 and 2721 MPa, respectively). But the addition of excessive La_2O_3 (>0.9 wt.%) particle reduces the bending strength and fracture toughness of Mo-12Si-8.5B alloy. Thus, different La_2O_3 contents are very sensitive to the strengthen and toughness of Mo-Si-B alloy [87]. According to the Griffith theory, critical stress (σ_c) formula for crack instability propagation is written as follows [88]:

$$\sigma_c = \sqrt{\frac{2E\gamma_S}{\pi\alpha}} \tag{4}$$

Here, E is the elastic modulus, γ_S is the surface energy and α is the half the length of the internal crack. We found that the doping of La_2O_3 particles can control the grain size and obtain smaller internal cracks. On the other hand, the dislocation movement is pinned by La_2O_3 particles to alleviate the dislocation accumulation and stress/strain concentration at the GBs, making it more difficult to generate and expand microcracks at the GBs [89], thus greatly improving the toughness of Mo-12Si-8.5B alloy. For fine-grained Mo-12Si-8.5B alloy with bimodal α-Mo grains, the nano La_2O_3 content on α-Mo grains has a strong toughening effect [90]. And the microcracks toughening induce by La_2O_3 particles played a more effective role in coarse-grained (CG) α-Mo regions. Specifically, the critical fracture toughness value (K_{IC}) commonly used in engineering is given as follows [91,92]:

$$K_{IC} = \sqrt{\frac{EG_{IC}}{1-\vartheta^2}} \tag{5}$$

where E is Young's modulus, ϑ is Poisson's ratio, and $G_{IC} = W/A$ is the work W during fracture divided by the crack swept area A. For Mo-12Si-8.5B alloy, the fracture toughness value (K_{IC}) can be represented as follows [93]:

$$K_{IC} \approx K_c^b\left\{1 + \frac{2r}{l}\left[\left(\frac{K_c^d}{K_c^b} - 1\right)\right]\right\}^{1/2} \tag{6}$$

where the K_{IC} is the fracture toughness of the "Mo-Si-B composite", K_c^d is the relative toughness of the ductile α-Mo phase region

Table 1
Fracture toughness prediction based on crack trapping. Adapted with permission from Refs. [90,96]. Reprinted from Materials Science & Engineering A, 5500780344268, Copyright (2020), with permission from Elsevier. Reprinted from International Journal of Refractory Metals and Hard Materials, 5500781372581, Copyright (2021), with permission from Elsevier.

Samples	l (μm)			r (μm)	Calculated toughness, K_{IC} (MPa m$^{1/2}$)	Experimental toughness, K_q (MPa m$^{1/2}$)
	Minimum, l_{min}	Maximum, l_{max}	Average, l_{ave}			
HEBMed	4.2	17.7	11.21	1.2	7.43	9.20
HEBMed+ unmilled 10 wt.% Mo-La_2O_3	3.1	10.9	7.18	1.54	10.08	11.25
HEBMed+ unmilled 15 wt.% Mo-La_2O_3	3.0	10.0	6.30	1.79	11.48	12.50
HEBMed+ unmilled 20 wt.% Mo-La_2O_3	3.0	10.4	6.55	1.81	11.33	11.53
HEBMed+ unmilled 20 wt.% Mo-La_2O_3–1700	2.7	8.5	5.23	1.83	12.66	13.03
HEBMed+ unmilled 20 wt.% Mo-La_2O_3–1800	2.5	8.0	5.15	1.90	12.98	13.41

taken as 15 MPa m$^{1/2}$[94], K_c^b is relative toughness of the brittle intermetallic (Mo_3Si/Mo_5SiB_2) phases region as ~3 MPa m$^{1/2}$ [95]. The r and l are characteristic size of α-Mo phases area and its average spacing, respectively. The calculated fracture toughness (K_{IC}) of Mo-12Si-8.5B alloy is shown in Table 1, and the toughening and strengthening mechanism of bimodal structure is quantitatively analyzed [90,96]. The results show that the fracture toughness of CG-Mo (36.19 vol%) with La_2O_3 powders is significantly improved (increased by about 36%). To further optimize the fracture toughness of bimodal Mo-Si-B alloy, the alloy with 20 wt% La_2O_3 powder is annealed at 1700 °C and 1800 °C. Due to the additional toughening from the formation of microcracks induced by La_2O_3 powders, the fracture toughness (K_q) reaches 13.41 MPa m$^{1/2}$.

The room-temperature fatigue properties of Mo alloys doped with La_2O_3 particles were also developed in Ref. [97]. The low-cycle fatigue (LCF) test showed that the alloy containing La_2O_3 particles obtained by the solid-liquid mixing method and pressureless sintering technology had cyclic softening behavior, high fatigue ductility, and the longest cyclic fatigue life. To better evaluate the LCF behavior of PM and Mo-La_2O_3 alloys, they used the Basquin-Manson-Coffin (BMC) relationship to analyze the elasticity, plasticity, and total strain amplitudes and failure inversion time ($2N_f$). The BMC model [98] is:

$$\varepsilon_a = \frac{\sigma'_f}{E}(2N_f)^b + \varepsilon'_f(2N_f)^c \tag{7}$$

where σ'_f is the fatigue strength coefficient, E is the elastic modulus, b is the fatigue strength index, and ε'_f and c are the fatigue ductility coefficient and the fatigue ductility index, respectively. It is calculated using Eq. (7) that pure Mo has the lowest fatigue ductility coefficient (ε'_f), and ε'_f for the Mo alloy containing La_2O_3 particles increases significantly, indicating that Mo-La_2O_3 has good fatigue resistance.

In addition to the room temperature mechanical properties, the effect of high-temperature mechanical performance of the Mo alloy with La_2O_3 particle addition is also proposed [99–102]. Li et al. [103] studied the high temperature compression behavior of FG (unimodal) and bimodal Mo-12Si-8.5B-0.57 wt.% La_2O_3 alloy. They focused on the deformation and dynamic recrystallization behavior of Mo-12Si-8.5B-0.57 wt% La_2O_3 alloy. Nanoscale La_2O_3 particles strengthened the Mo-12Si-8.5B alloy at high temperatures (1000–1400 °C) by inhibiting dislocation slip and pinning GBs. Compared with FG (unimodal) alloy, the compressive strength and yield strength of the bimodal alloy at 1400 °C are increased by 55.2% and 43.6%, respectively. To reveal the effect of La_2O_3 content on the deformation of the Mo alloy at high temperature, Cheng et al. [104] explored the strengthening mechanism of Mo-xLa_2O_3 alloy with different contents (x = 0 wt%, 0.5 wt%, 1.0 wt%, 1.5 wt% and 2.0 wt%). The results suggest that the plastic deformation and strength of the Mo alloy with La_2O_3 addition of 1.0 wt.%–1.5 wt.% increase significantly. However, severe strain softening occurs in Mo-2.5% La_2O_3 alloy. The critical strain ε_v of particles in metal matrix expresses as [105]:

$$\varepsilon_v = \left(\frac{Gb + G_p b_p}{KE_p d_{intra}}\right) \tag{8}$$

where G_p, E_p and b_p are the shear modulus (180 GPa), Young's modulus (330 GPa), and Burgers vector (0.31 nm) of La_2O_3 particles, respectively. The K is a constant. The Weibull expression is as follows [106]:

$$P_c = 1 - \exp\left[-\frac{f_{intra}}{f_o}\left(\frac{\varepsilon}{\varepsilon_v}\right)^m\right] \tag{9}$$

where P_c is the percentage of debonding intragranular particles, the f_o is the reference particle volume fraction that caused 63.2% interfacial debonding under the equal load (ε_v). The ε_v is obtained by Eq. (8) as approximately ~8% in the Mo-1.0 wt% La_2O_3 and Mo-1.5 wt% La_2O_3 alloys. Therefore, up to 20% of the particles in the grains degummed and cause damage, resulting in competition between micropores and microcracks (Fig. A.1 in Supplementary Materials), which leads to strain softening in the Mo alloys. It is demonstrated that high temperature strength-elongation combination is the most favorable in Mo-La_2O_3 alloy with La_2O_3 between 1.0 and 1.5 wt.%.

Compared with high temperature compression, the high temperature creep properties of Mo- La_2O_3 alloy have also been discussed. Cheng et al. [107] added 0.6, 0.9, and 1.5 wt.% La_2O_3 particles by PM to explore the high-temperature creep properties of Mo alloys. The Mo and Mo-La_2O_3 alloys are tested under constant load tensile creep at temperatures ranging from 1000 °C to 1400 °C (Fig. A.2 in Supplementary Materials). where the creep stress index and activation energy are estimated based on the measured creep rate data. The stress index of pure Mo is about 5.6 in Fig. 2(a). The Mo-La_2O_3 alloy has a high stress index value, ranging from 10 to 20 in Fig. 2(b–d), and its apparent activation energy is between 430 kJ/mol and 760 kJ/mol. Based on the creep constitutive model of the interaction between particles and dislocations, when dislocations bypass La_2O_3 particles, with the increase of the volume fraction of La_2O_3 particles and the decrease of particle size, the climbing resistance increases, which makes the energy relaxation efficiency of dislocation lines lower. This shows that the doped nano-La_2O_3 changes the creep behavior of the Mo alloy. They propose a creep constitutive model based on particle and dislocation interactions. The relationship between creep rate and creep strength is [108]:

$$\frac{\dot{\varepsilon}}{D_V} = \frac{6\lambda\rho}{b}\exp\left(-Gb^2 r\frac{\left[(1-K)\left(1-\frac{\sigma}{\sigma_d}\right)\right]^{\frac{3}{2}}}{k_B T}\right) \tag{10}$$

Here, r and λ are the particle radius and the average particle spacing, respectively, ρ is the dislocation density. G is the shear modulus, D_V is the diffusion coefficient, b is the Burgers vector, k_B is the Boltzmann constant, and K is the relaxation parameter

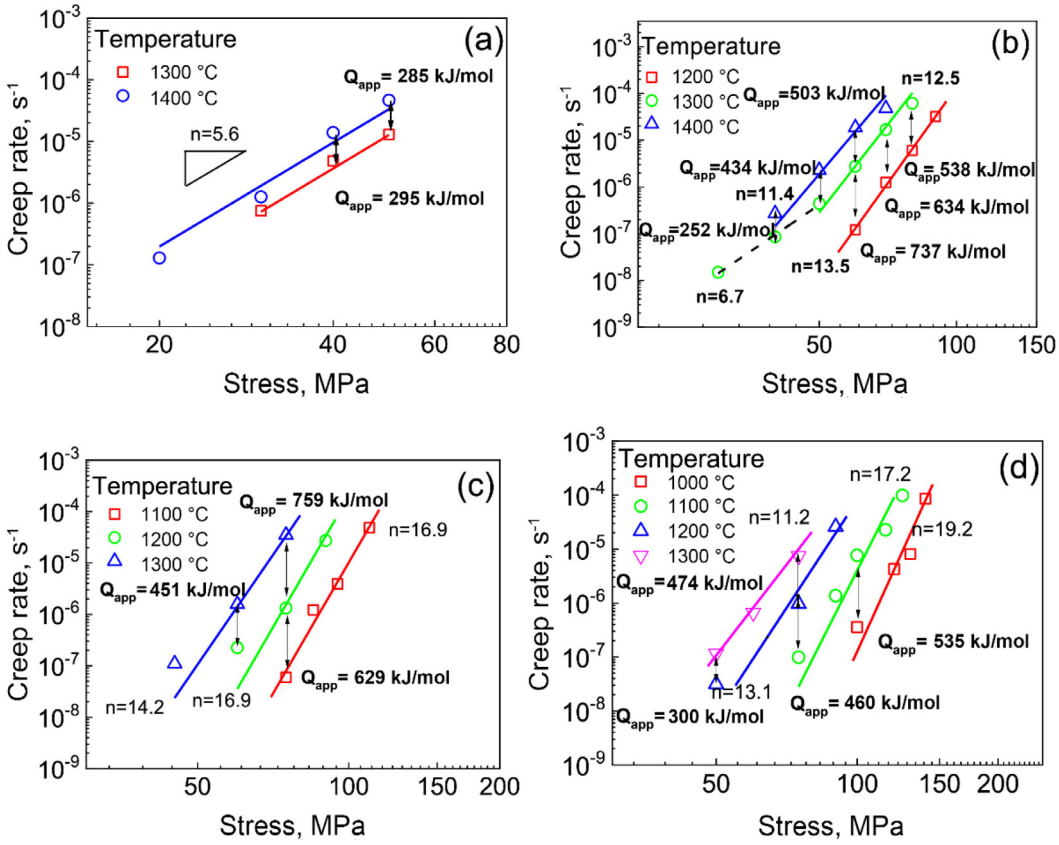

Fig. 2. Double logarithm plots of steady creep rate vs. stress relation at different temperatures: (a) pure Mo, (b) Mo-0.6 wt.% La_2O_3, (c) Mo-0.9 wt.% La_2O_3, (d) Mo-1.5 wt.% La_2O_3. Adapted with permission from Ref. [107]. Reprinted from Journal of Materials Science & Technology, 5411790332641, Copyright (2022), with permission from Elsevier.

of the dislocation. Compared to other dispersion-strengthened alloys, Mo alloys with La_2O_3 particles has a higher relaxation factor K, so the relaxation dislocation line energy is quite low. While increasing the volume fraction of La_2O_3 or refining the nanoparticles leads to a larger $1\lambda - r$, which enhances climbing resistance. Thus, the Mo alloy with 1.5 wt.% La_2O_3 has the highest creep strength. By changing the size and distribution of La_2O_3 particles, Mo-La_2O_3 alloy with improved creep strength can be designed, which is of great reference value and guiding significance for future research.

It is known that adding rare earth elements is a potential method to improve the corrosion resistance of Mo [109,110], but there are only a few studies on the corrosion resistance properties with added rare earth La_2O_3 oxides. The La_2O_3 affects the chemical properties (corrosion and oxidation resistance) of Mo alloys. Cairang et al. [111] characterized the corrosion behavior of pure Mo and Mo alloy doped with 0.3 wt.% La_2O_3 in 3.5 wt.% NaCl solution at 25 °C by potentiodynamic polarization measurements, electrochemical impedance spectroscopy (EIS), and linear polarization resistance (LPR). In Fig. 3, oxide films are formed on the surfaces of pure Mo and doped Mo samples, and the current density of doped Mo is much smaller than that of pure Mo, indicating that the corrosion resistance of Mo doped with La_2O_3 is better than pure Mo. Electrochemical impedance spectroscopy results show that the resistance of the Mo surface oxide film doped with La_2O_3 increases, and it improves the stability of the Mo surface oxide film, which make Mo-La_2O_3 more effective in protecting the matrix from corrosion. Further experiments are carried out on the linear polarization resistance (LPR) of pure Mo and Mo-La_2O_3 alloy in 3.5 wt.% NaCl aerated solution at 25 °C (Fig. A.3 in Supplementary Materials). By measuring the polarization resistance R_p at different times, it has been seen that the polarization resistance of doped Mo is more pronounced than pure Mo. Thus, the addition of La_2O_3 can promote the formation of a more compact and protective oxide film, which greatly improves the corrosion resistance and provides a good design for improving the corrosion resistance of Mo alloy. Doping with La_2O_3 can significantly improve oxidation resistance.

In addition, doping with La_2O_3 in Mo can significantly improve the oxidation resistance. Some theoretical studies [112–114] have demonstrated the improved oxidation resistance of Mo alloys by adding rare earth La_2O_3 particles. In Ref. [115] the oxidation mechanism formation of La_2O_3-doped Mo-12Si-8.5B alloy was studied. Isothermal oxidation tests have shown that the oxidation resistance of Mo-12Si-8.5B alloy is positively affected by the doping of lanthanum oxide, and the oxidation resistance of Mo-12Si-8.5B alloy with 0.3 wt.% and 0.6 wt.% La_2O_3 is significantly enhanced. La_2O_3 doping can promote tight bonding between the crystal and the interlayer.

The above experiment results show that the addition of La_2O_3 particles is an effective approach to design the high-performance Mo alloy. The La_2O_3 particles dispersion-strengthened could significantly control the grain size of Mo alloys and increase the room-temperature properties, high-temperature properties and chemical properties in Mo alloys. Through different preparation methods, such as mechanical alloying, freeze-drying combined with hot-pressing sintering, or pressureless sintering, La_2O_3 particles with high sintering activity can be obtained, so that the minimum size of La_2O_3 particles concentrates at 2–5 nm and uniformly distributes in Mo grains interior. The crystallinity and particle size of Mo powder are changed by high activity La_2O_3 particles. As a matter of fact, the La_2O_3 particle volume fraction, particle size, and distribution are the main factors affecting the microstructure and strengthening mechanism of Mo alloy. Highly active and ultrafine size La_2O_3 particles are uniformly distributed around the

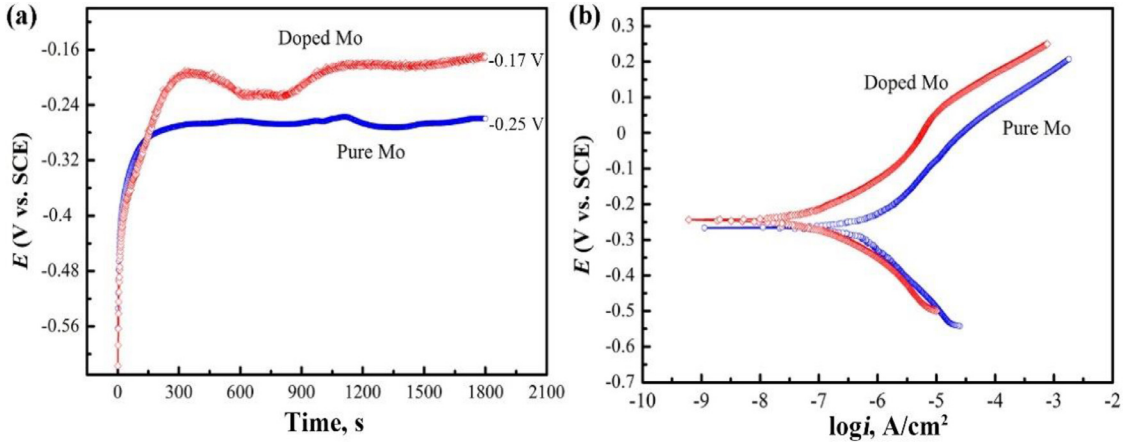

Fig. 3. (a) The open circuit potential and (b) potentiodynamic polarization curves of pure Mo and doped Mo in aerated 3.5 wt.% NaCl solution at 25 °C. Adapted with permission from Ref. [111]. Reprinted from Corrosion Science, 5411791228973, Copyright (2022), with permission from Elsevier.

grain boundary of the Mo alloy, which can effectively enhance the Zener force and interfacial resistance, hinder dislocation slips and grain boundary movement, and reduce dislocation density. The freeze-drying technology provides an excellent solution for creating the ultra-fine size and high sintering activity of nano-sized La_2O_3 particles and composite powders. And the Mo grains are refined to 440 nm with high hardness (495 $HV_{0.2}$), and strength (1201 MPa) at 30% strain. By mechanical alloying combined with the hot-pressing sintering process, the addition of La_2O_3 particles into Mo-12Si-8.5B alloy can have better room temperature compressive strength (2806 MPa) and yield strength (2721 MPa). The addition of La_2O_3 particles can greatly enhance the high temperature creep resistance, corrosion resistance, and oxidation resistance of Mo alloy. In addition, there are few reports on the high temperature strength and toughness of Mo alloys with La_2O_3 particles, and the contribution of the particles to the strength and toughness of Mo alloy needs to be improved. In the next work, it will be necessary to investigate the mathematical modeling and prediction of the effect of La_2O_3 particles on the creep resistance of Mo alloys at high temperatures.

2.2. Doped with Y_2O_3 particles

Compared with carbide particles, rare earth oxide particles can be formed in situ in alloys [116], refining grains and effectively improving their strength and toughness [117]. Mo alloys prepared by the mechanical alloying method have coarse Mo grains and large oxide particles at the GBs. To synthesize high-quality ultrafine ODS-Mo powders with high relative density and ultrafine grains, many researchers focus on sol-gel [118], hydrothermal synthesis [119], and freeze-drying methods [120] to precisely control the size, morphology, and purity of oxide powders. Rare earth Y_2O_3 particles are considered an ideal dispersant, and its can be applied to the development of oxide dispersion-strengthened alloys to ensure mixing at the molecular level [68,121,122], and obtain high-purity nano precursors for refining alloys [123,124], improving their grain size uniformity, comprehensive mechanical properties [125–127] and radiation resistance [128]. These guide the preparation of high-quality molybdenum alloys in the future. The information about the preparation of Mo-Y_2O_3 particles is summarized by utilizing the latest freeze-drying method and hydrothermal synthesis method, thereby obtaining the Mo alloy with excellent comprehensive mechanical properties.

It is well known that freeze-drying (FD) is a promising method, which can achieve a remarkable balance between ultrafine particles and the relative density of alloy [124,129]. Hu et al. [130] prepared Mo-Y_2O_3 particles with a 54 nm size and Mo-Y_2O_3 alloy with the smallest grain size of 620 nm and high density (99.6%) by this method and compared them with the ball milling method (BM). Most of the oxide particles of FD-Mo are dispersed inside the Mo grains. They further explored the reason for the uniform distribution of Y_2O_3 particles and found that Y_2O_3 powders could be formed in situ in GBs during the powder preparation process. The existence of the mixed phases of $Y_5Mo_2O_{12}$ and Y_2O_3 are observed by transmission electron microscopy (TEM), which indicates that Y_2O_3 could diffuse into Mo grains to form the $Y_5Mo_2O_{12}$ phase during high-temperature sintering. The formation of $Y_5Mo_2O_{12}$ particles is explained in Fig. 4. It was the formation of $Y_5Mo_2O_{12}$ particles that can adsorb more oxygen impurities near the Y_2O_3 particles, which can purify the Mo matrix, thereby improving the mechanical properties of the alloy, including the alloy with a high hardness of 487±28 $HV_{0.2}$, high yield strength of 902 MPa and high compressive strength of 1110 MPa.

The preparation of high-quality composite precursor powders by hydrothermal synthesis plays an important role in ODS-Mo alloys [68] because this method can greatly facilitate the distribution of Y_2O_3 particles into the grains, thereby achieving a balance of strength and ductility. Recently, the chemical reaction, phase formation refinement mechanism, and morphological evolution of Mo powder for the hydrothermal synthesis of Y_2O_3 and Mo powder precursors have received much more attention. In Ref. [131], the Mo-Y_2O_3 composite precursor powder was prepared by hydrothermal synthesis and two-step hydrogen reduction. The particle size in Mo-Y_2O_3 mixed powder and the reason for Mo grain refinement are analyzed. From the measurement of particle size of two-stage reduction powder, both the particle size and grain size of powders decrease significantly after adding 1 wt.% Y_2O_3, as seen in Fig. 5. The particle size D_{50} decreases to 4.97 μm in the first stage and 3.9 μm in the second stage. To elucidate the refinement mechanism of Y_2O_3 on the reduced powder, they also calculated the two-dimensional lattice mismatch at the interface between Y_2O_3 and Mo. From the calculation of the lattice mismatch degree [132] between the low-index (1 0 0), (1 1 0), and (1 1 1) crystal planes in the Mo/Y_2O_3 interface, it is clear from Table 2 that the lattice mismatch degree at the Mo/Y_2O_3 interface is less than 15%. This indicates that Y_2O_3 particles can act as heterogeneous nucleation sites for Mo, further ensuring the refinement and homogenization of mixed powders, and becoming heterogeneous nucleation sites in the Mo matrix (Fig. A.4 in Supplementary Materials). The high density of Mo-Y_2O_3 alloy and the prevention of grain growth are achieved by using the spark plasma sintering (SPS) technique with the advantages of short time and low sintering temperature [133–

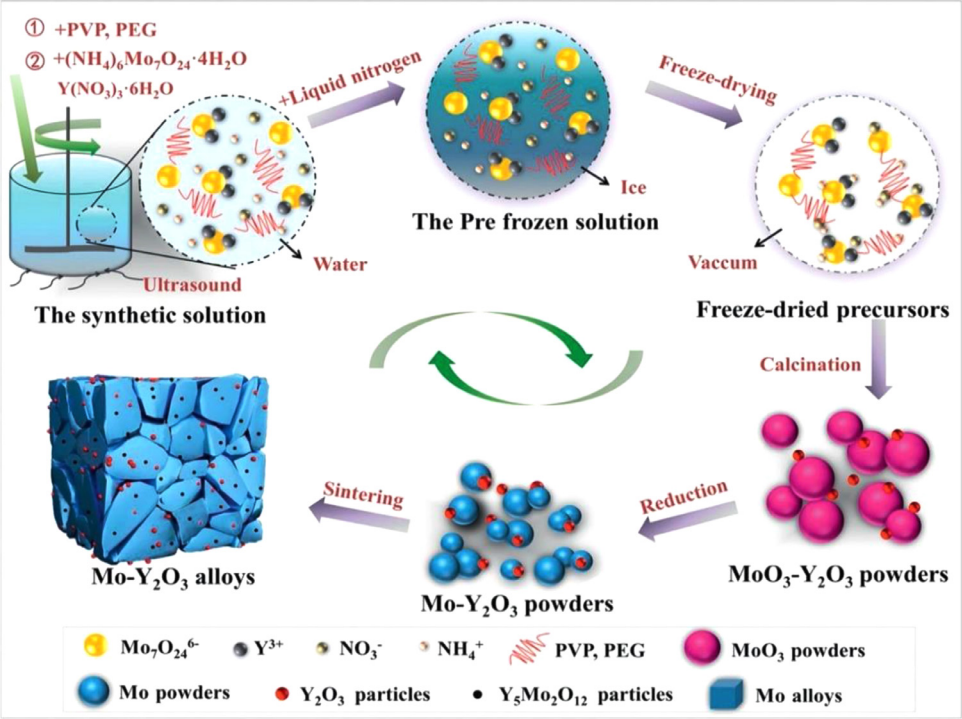

Fig. 4. Schematic diagram of the freeze-drying process. Adapted with permission from Ref. [130]. Reprinted from Journal of Materials Science & Technology, 5411801101817, Copyright (2021), with permission from Elsevier.

Table 2
The two-dimensional lattice mismatch between Y_2O_3 and Mo. Adapted with permission from Ref. [131]. Reprinted from International Journal of Refractory Metals and Hard Materials, 5,411,810,715,536, Copyright (2021), with permission from Elsevier.

Matching interface	[*uvw*]s	[*uvw*]n	d[*uvw*]s	d[*uvw*]n	θ	δ	$\delta(hkl)$n(hkl)s
(100)Y_2O_3//(100)Mo	[010]	[010]	10.601	3.147	0	10.94	10.94%
	[011]	[011]	14.992	4.451	0	10.93	
	[001]	[001]	10.601	3.147	0	10.94	
(110)Y_2O_3//(110)Mo	[110]	[1$\bar{1}$0]	14.992	4.451	0	10.93	10.94%
	[1$\bar{1}$1]	[1$\bar{1}$1]	9.181	2.725	0	10.96	
	[001]	[001]	10.601	3.147	0	10.94	
(111)Y_2O_3//(111)Mo	[$\bar{1}$10]	[$\bar{1}$10]	14.992	4.451	0	10.93	10.93%
	[$\bar{2}$11]	[$\bar{2}$11]	25.967	7.709	0	10.93	
	[$\bar{1}$01]	[$\bar{1}$01]	14.992	4.451	0	10.93	

135]. Therefore, Y_2O_3 particles can be used as heterogeneous nucleation sites of Mo alloys to ensure nucleation during the reduction of mixed powders, reduction of agglomerated grains, and uniformity of the size of composite precursor powders. The results of this study provide a valuable reference for the preparation of Y_2O_3-doped Mo alloys by optimizing the hydrothermal parameters and SPS sintering method in the future.

The adding Y_2O_3 particles of the Mo alloy also can obtain better mechanical properties of Mo alloys [136,137]. For example, Xu et al. [138] paid more attention to the effects of Y_2O_3 particles and CeO_2 co-doping on the mechanical properties. They synthesized composite powders with different contents of Y_2O_3 and CeO_2 by hydrothermal method and obtained rolled Mo alloy with almost no recrystallized grains by pressureless sintering. The tensile properties, strength-ductility balance, and tensile fracture morphology of the Mo alloy plate are analyzed in Fig. 6. With the increase of Y_2O_3 content, the tensile strength of the Mo alloy sheet increases, while the elongation increases first and then decreases in Fig. 6(a). The tensile strength and elongation reach the maximum values of 917 MPa and 18% when the Y_2O_3 contents are 0.8 wt.% and 0.3 wt.%, respectively. For the Mo-0.8% Y_2O_3–0.12% CeO_2 alloy anneals at 850 °C, the tensile strength can reach 853 MPa, and the elongation decreases to 15%. When the annealing temperature increases to 1200 °C, the tensile strength decreases sharply, but the elongation after fracture will increase. Through the comprehensive analysis, it can be indicated that the Mo alloy with 0.5% Y_2O_3 and 0.12% CeO_2 have excellent comprehensive mechanical performance. Comparing the strength, ductility, and strength-elongation product ($P_{st} = \sigma_b\delta$) of different rolled Mo alloys, as shown in Fig. 7, the strength-elongation of the newly developed Mo alloy can reach 15,000 MPa.%, in which the Y_2O_3 nanoparticles are the main reason for improving strength and plasticity (Orowan and fine-grain strengthening [139]). Similarly, Y_2O_3 is added to Mo-Ni alloy by mechanical alloying and pressureless sintering (1500 °C for 2 h) [140]. The Mo-Ni-Y_2O_3 alloy has a good effect on oxide dispersion and grain refinement. The average hardness of Y_2O_3-doped Mo-Ni alloy is 8.73 GPa, which is higher than that of pure Mo (~2.82 GPa). For Mo-3Si-1B alloys, which are expected to replace nickel-based high temperature alloys [141], the addition of Y_2O_3 has a significant effect on the fracture toughness and oxidation resistance of the alloy. The fracture toughness of the Mo-3Si-1B-1Zr-1 Y_2O_3 alloy with a continuous α-Mo matrix can reach an average value of 13.5 MPa $m^{1/2}$. Adding 8.2 wt.% and 5.0 wt.% ZrO_2 (Y_2O_3)

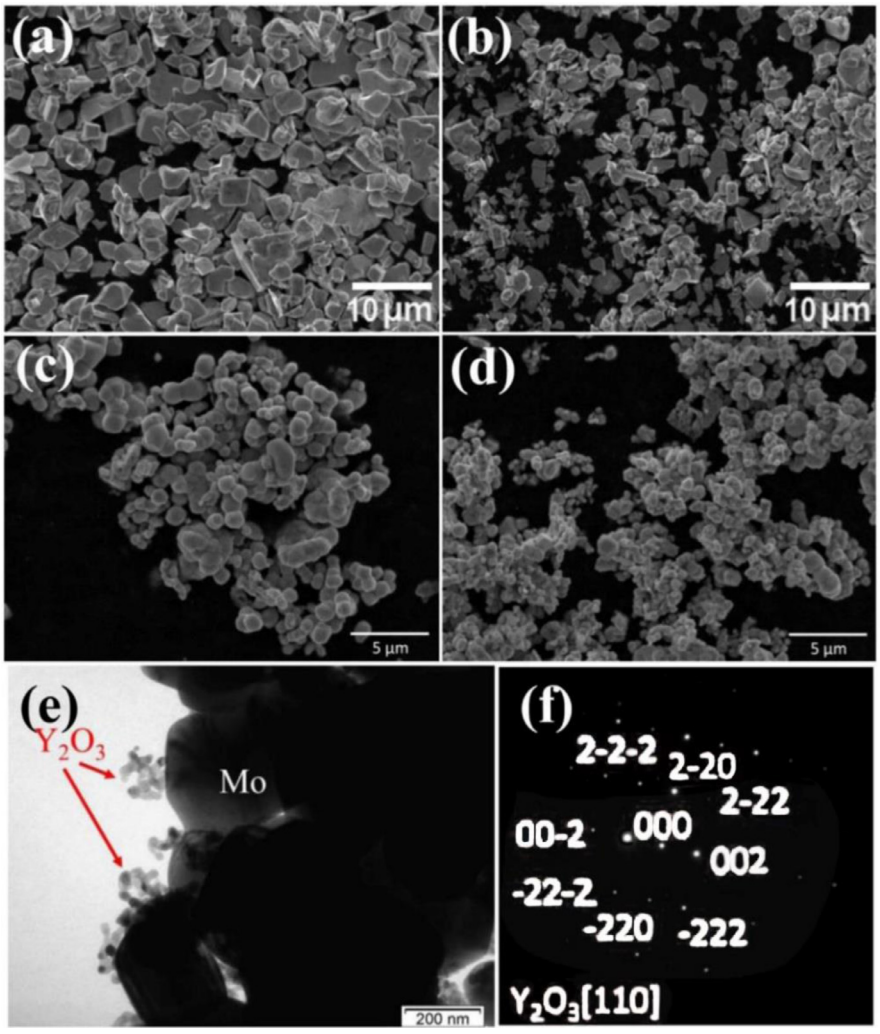

Fig. 5. SEM micrographs of the powders: (a) #0 and (b) #1 after the first stage of reduction, (c) #0 and (d) #1 after the second stage of reduction, (e) TEM images showing the morphology of the reduced powders #1, and (f) selected diffraction spots of the surrounded particles with a mean diameter in 18.6 nm. Adapted with permission from Ref. [131]. Reprinted from International Journal of Refractory Metals and Hard Materials, 5411810715536, Copyright (2021), with permission from Elsevier.

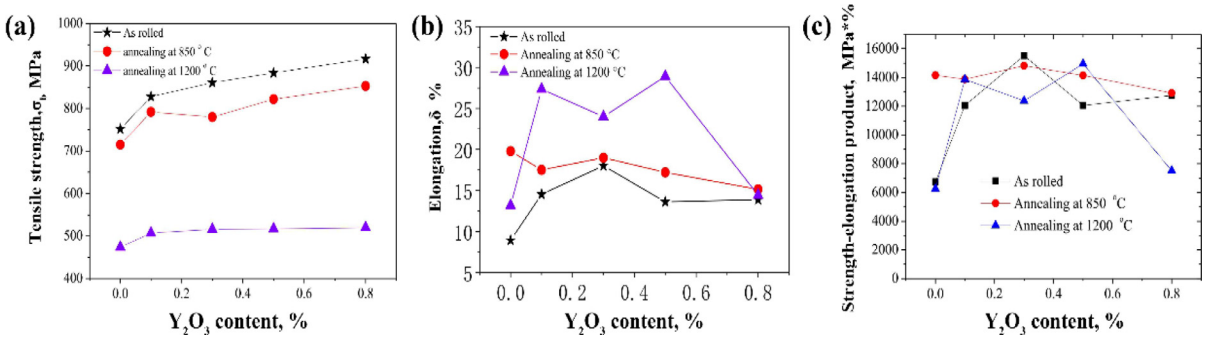

Fig. 6. Effects of Y_2O_3 content on (a) tensile strength, (b) elongation, and (c) strength-elongation product of the Mo alloy plates under different states. Adapted with permission from Ref. [138]. Reprinted from Journal of Alloys and Compounds, 5411811271999, Copyright (2022), with permission from Elsevier.

powder into Mo-12Si-8.5B alloy, the fracture toughness increases to 12.82 MPa $m^{1/2}$ and 12.38 MPa $m^{1/2}$, respectively [142].

To sum up, the Mo-Y_2O_3 alloy plays a very dominant role in the excellent hardness, yield strength, compressive strength, and fracture toughness. By Y_2O_3 particles doped by different preparation methods, such as freeze-drying, hydrothermal synthesis, and powder ball milling alloying, high-quality ultrafine composite powders with high sintering activity can be synthesized. The size (20–50 nm) and purity of Y_2O_3 particles are precisely controlled. These are the most important factors of Y_2O_3 particles affecting the microstructure of Mo alloys. When Y_2O_3 has a small aspect ratio, the interaction between particles and dislocations is similar to that of spherical Y_2O_3. The dislocation ring in Mo alloy either exists around the particles or bypasses the nano-Y_2O_3 particles by changing the propagation direction to reduce the stress concentration and microcracks, resulting in a better strengthening effect [143]. Recent research has found that the powder particles prepared by the freeze-drying method not only control the size and uniform

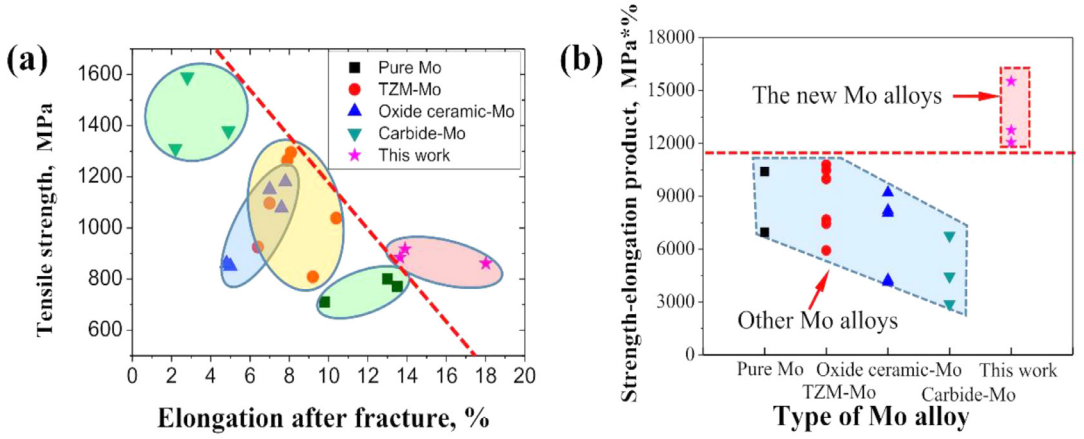

Fig. 7. Comparison of strength and ductility (a) and strength-elongation (b) product of different rolled Mo alloys. Adapted with permission from Ref. [138]. Reprinted from Journal of Alloys and Compounds, 5,411,811,271,999, Copyright (2022), with permission from Elsevier.

distribution of the powder, but also $Y_5Mo_2O_{12}$ particles generates by ultrafine Y_2O_3 particles (about < 50 nm), which absorbs O impurities and purify the Mo matrix. Then the Mo alloy has the finest grain size (620 nm), high density (99.6%), high hardness 487 ± 28 $HV_{0.2}$, high yield strength 902 MPa, and high compressive strength 1110 MPa. The Mo-Y_2O_3 alloy is produced by the combination of the hydrothermal synthesis method and SPS sintering ensures the fineness and uniformity of the mixed powder. Particularly, Y_2O_3 particles can act as heterogeneous nucleation sites for the Mo matrix, further ensuring the reduction of agglomerated grains and finally obtaining high quality composite precursor powders with fine grains and best homogeneity. And it obtains high quality composite precursor powders with fine particles and optimal homogeneity. The addition of Y_2O_3 to Mo alloy through mechanical alloying and pressureless sintering has a high hardness of 8.73 GPa, which is expected to replace nickel-based superalloys. Compared with traditional PM preparation methods, these two preparation methods can better control the size, purity, and uniformity of doped Y_2O_3 powder. More attention has been paid to Y_2O_3 particle-doped dispersion strengthened Mo alloys. However, through different preparation methods, the strengthening potential of Y_2O_3-doped Mo alloy at high temperatures is under investigation.

2.3. Doped with Al_2O_3 ceramic particles

Al_2O_3 ceramic particles have high hardness and wear resistance, strong corrosion resistance, and good heat resistance. It is an oxide with the most stable chemical properties and the highest mechanical strength of refractory oxides. It is usually used as reinforcing particles to enhance the properties of metallic materials [144–148]. Adding Al_2O_3 ceramic particles to Mo alloys results in excellent high-temperature wear resistance, high strength, and hardness. Xu's team successfully prepares Mo alloys doped with different volume fractions of Al_2O_3 particles by sol-gel [149–151] and hydrothermal methods [152]. The Al_2O_3 particles can be uniformly distributed along the grain boundary and well bonded with the Mo matrix. They also reported that the preparation of Mo alloys reinforced with in-situ α-Al_2O_3 particles proved that α-Al_2O_3 can improve the wear resistance of Mo alloys [153]. The synthesized Al_2O_3 ceramic particles are mostly prepared by pressing and pressureless sintering. In this paper, the volume fraction and particle size of Al_2O_3 particles have been studied, mainly considering the effects of grain size, room-temperature, and high-temperature mechanical properties of Al_2O_3 particle doped dispersion strengthened Mo alloy.

The Al_2O_3 ceramic particles may effectively control the grain size [154], which is very important for the properties of the Mo alloy [151]. The grain size and hardness are greatly affected by different Al_2O_3 content. Mo-Al_2O_3 alloy was prepared in Ref. [155] by adding Al_2O_3 powder using mechanical ball milling and pressureless sintering. In the ball milling process, Al_2O_3 nanoparticles can be uniformly dispersed with Mo particles, and the particle size of Mo decreased with the Al_2O_3 content. When the content of Al_2O_3 particles is less than 20 wt.%, it has a pinning effect on the Mo matrix, which reduces the relative density. The content of Al_2O_3 greater than 20 wt.% is beneficial to eliminating the pores of the Mo matrix and increases the relative density, thereby accelerating the densification behavior. When Al_2O_3 content is increased from 0 to 30 wt.%, it is obvious that the grain size decreases sharply, as seen in Fig. 8(a–f). The grain size of pure Mo changes from 17.9 μm to 1.65 μm for the Mo-30 wt.% Al_2O_3, and the grain size decreases by nearly 11 times. As the content of Al_2O_3 particles increases, the diffusion of Mo atoms is hindered, and the growth of Mo grains becomes difficult. They also demonstrated that the hardness of the Mo-Al_2O_3 cermet increased from 164.2 HV to 464.3 HV due to the higher hardness of Al_2O_3 than the Mo matrix. Nanostructured Mo-Al_2O_3 alloys with high hardness (385 HV) were obtained in Ref. [156]. The prepared doped nano-Al_2O_3 powder has high sintering activity, and the relative density of Mo alloy reaches more than 95.4% under pressureless sintering (sintering at 1300 °C for 3 h). It turned out that Al_2O_3 can significantly affect the microstructure and hardness of Mo alloys. This synthesis method and preparation sintering technology also have great potential in the industrial application of nanostructured Mo alloys.

Notably, the Al_2O_3 ceramic particles can improve the mechanical properties of Mo alloys [157]. The quantitative effects of Al_2O_3 nanoparticles on the mechanical properties, including microhardness, elastic modulus, and yield strength of Mo alloy were analyzed in Ref. [158]. They fabricated Al_2O_3 particles with different volume fractions by hydrothermal method, and carried out isostatically cold pressing and pressureless sintering at 1900 °C for 3 h. It obtains that the highest yield strength of Mo-1.28 vol.% Al_2O_3 alloy is 859 MPa. The quantitative yield strength model related to Al_2O_3 particles and annealing temperature was established [159,160]. First, the yield strength (σ_y) of the Mo alloy plate doped with Al_2O_3 particles can be expressed as:

$$\sigma_y = \sigma_m + \kappa / D^{1/2} + \sigma_p \quad (11)$$

Here, k is a constant of the Hall-Petch slope and D is the grain size of Mo. Then according to the Orowan-Ashby equation [139],

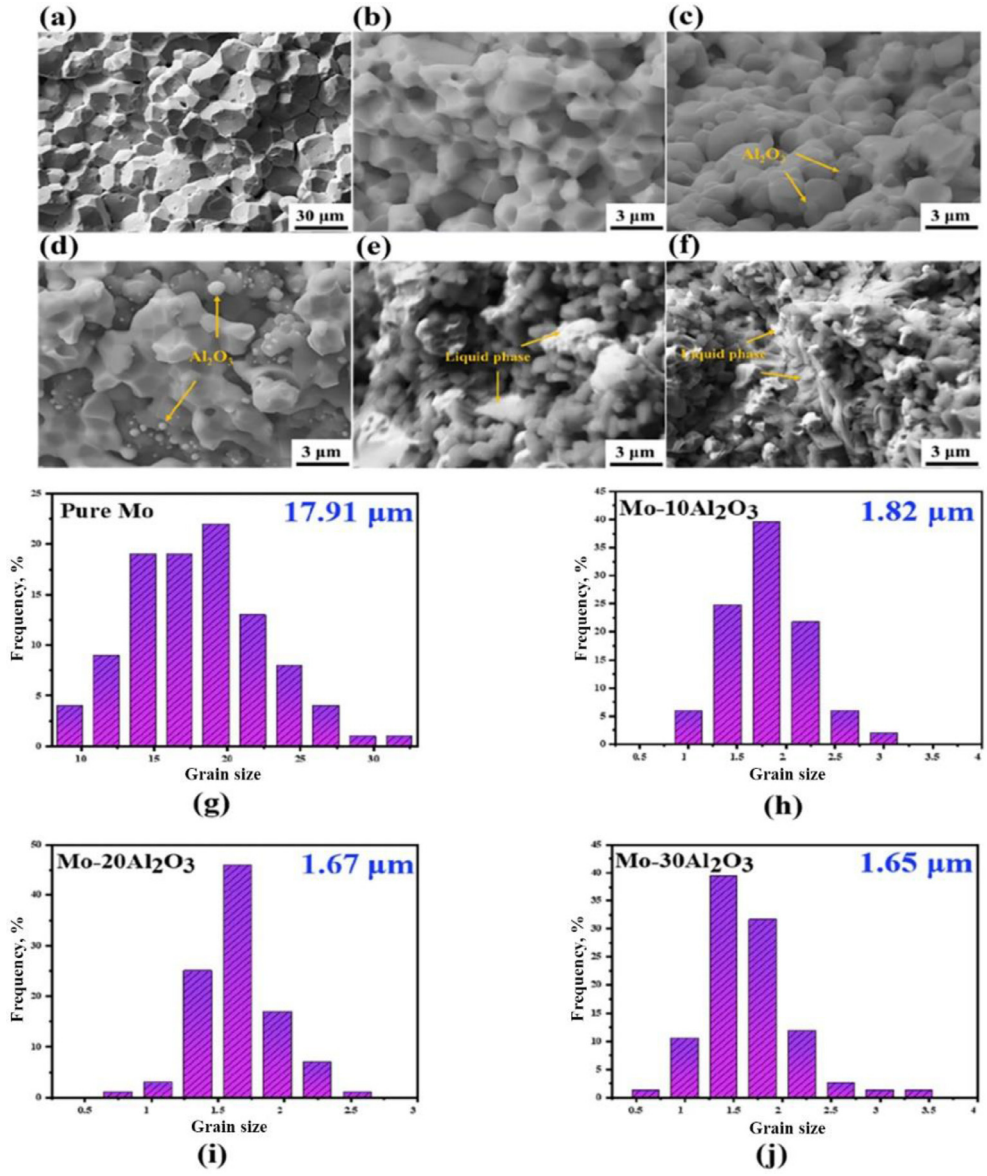

Fig. 8. Fracture morphology and grain size distribution of the sintered Mo-(Ni)-Al_2O_3 cermets: (a, g) pure Mo; (b, h) Mo-10 Al_2O_3; (c, i) Mo20Al_2O_3; (d, j) Mo-30 Al_2O_3; (e) Mo-5Ni-30 Al_2O_3; (f) Mo-10Ni-30Al_2O_3. Adapted with permission from Ref. [155]. Reprinted from The Minerals, Metals & Materials Society, 5411821391167, Copyright (2021), with permission from Springer.

Orowan strength is expressed as:

$$\sigma_p = \sigma_{OR} = \frac{m\mu b}{(1.18) \times 2\pi \cdot d \cdot \left(\sqrt{\frac{\pi}{6f}} - 1\right)} \ln\left(\frac{d}{2b}\right) \tag{12}$$

Here, m is the Taylor factor, $m = 2.5$, μ is the shear modulus, $\mu = 140$ GPa [161], b is Burgers vector, $b = 2.72 \times 10^{-10}$ m, d is Al_2O_3 particle size and f is Al_2O_3 volume fraction. The functions of σ_m and k are obtained by linear fitting:

$$\sigma_m = 1223.68 - 0.68 \times T \tag{13}$$

$$\kappa = 1606.71 - 1.2 \times T \tag{14}$$

The yield strength of Mo alloy plate doping different content of Al_2O_3 particles at different annealing temperatures is:

$$\sigma_y = 1223.68 - 0.68 \times T + \frac{1606.71 - 1.2 \times T}{\sqrt{D}} + \frac{12.85}{d \times \left(\sqrt{\frac{\pi}{6f}} - 1\right)} \ln\left(\frac{d}{5.44 \times 10^{-10}}\right) \tag{15}$$

The yield strength model shows that the combined effects of grain and Orowan strengthening are the main reason for the strengthening mechanism, and the effect of nano-sized Al_2O_3 on the mechanical properties of the Mo alloy is expounded. The compressive properties of Mo alloys containing Al_2O_3 particles had also been investigated [162]. The uniaxial compression tests are carried out at room temperature for Mo alloys doped with 0–2 vol.% Al_2O_3, the yield strength of these samples is 11.5%, 12.1%, and 56% higher than pure Mo under the same conditions, indicating that Al_2O_3 doping significantly improves the yield strength of the Mo alloy because of dislocation strengthening and good crystallization relationship.

To be suitable for the manufacturing of the Mo alloy parts used at high temperatures, the high-temperature mechanical behavior of the Mo alloy doped with Al_2O_3 particles is studied. Zhou et al. [163] reported the high temperature (up to 1300 °C) ten-

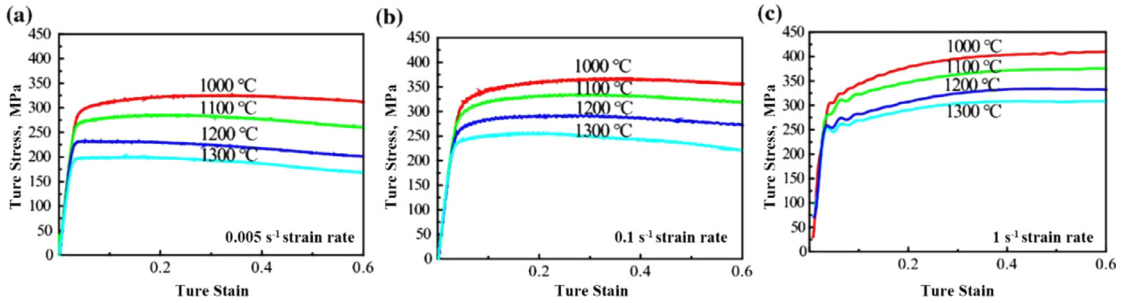

Fig. 9. True stress–strain curves of Mo-3 vol.% Al_2O_3 alloys at different temperatures at the strain rates of: (a) 0.005 s^{-1}, (b) 0.1 s^{-1} and (c) 1 s^{-1}. Adapted with permission from Ref. [167]. Reprinted from Metals and Materials International volume, 5411830633852, Copyright (2020), with permission from Springer.

sile properties and fracture morphology of Mo alloy sheets doped with 1.0 wt.% Al_2O_3 particles. They mainly observed the tensile strength and elongation of Mo samples tested at different temperatures. The fact that the tensile strength of Mo-Al_2O_3 alloy is 23%–62% higher than pure Mo sheet at 25–1300 °C, where the Mo alloy doped with 1 wt.% Al_2O_3 can obtain the maximum elongation at about 1200 °C. Since the size of Al_2O_3 particles remains unchanged at high temperatures, it maintains the enhancement effect at high temperatures for a long time, because the bonding between Al_2O_3 particles and Mo matrix is very good, therefore, doping with submicron and nanometer Al_2O_3 particles can hinder the recrystallization process by preventing grain boundary migration and dislocation movement [164]. In terms of high-temperature deformation, there are a lot of studies on the high-temperature mechanics of pure Mo and Mo alloys [165,166], while there are few studies on the high-temperature deformation behavior of Mo-Al_2O_3 doped with ceramic particles. Yao et al. [167] focused on the study of 3 vol.% Al_2O_3 particles' effects on the high-temperature thermal compression behavior of Mo alloys. They analyzed stress–strain curves for work-hardening, steady-state, and softening behavior at different strain rates (0.005 s^{-1}, 0.1 s^{-1}, and 1 s^{-1}) and high-temperatures (1000, 1100, 1200, and 1300 °C), and compared several constitutive models. First, three different types of flow curves can be obtained from Mo-3 vol.% Al_2O_3 alloys at three different strain rates: (i) the stress increases to the peak stress and then decreases with the strain in Fig. 9(a); (ii) the stress increases with the strain until stable stress is reached in Fig. 9(b); (iii) the phenomenon of continuous increases of stress with strain in Fig. 9(c). Second, in the process of plastic deformation, when the local stress of the Mo matrix exceeded the yield strength, dislocations would be generated and the stress can be converted into Al_2O_3 particles. The presence of a large number of dislocations increases further with the deformation, ultimately driving the plastic deformation of the compatibility between the Mo matrix and the Al_2O_3 particles in Fig. 9. Finally, the accurate prediction of its flow stress by the modified Arrhenius model is considered. In addition, by quantifying the work hardening rate, the work hardening rate of Mo-3 vol.%-Al_2O_3 alloy can be predicted more accurately (Fig. A.5 in Supplementary Materials). The Al_2O_3 particles distributed in the Mo matrix greatly enhance the compressive stress and have a higher elastic modulus, so it can strengthen the Mo alloy more effectively.

Based on the Mo alloys used under high-temperature conditions, it is necessary to evaluate their thermal fatigue resistance for reference in the design and material selection [101,168]. Corresponding research work has also been done on the thermal fatigue properties of Mo alloys doped with Al_2O_3 ceramic particles. Zhou et al. [169] conducted an in-depth study on the thermal fatigue properties of the Mo alloy sheets doped with Al_2O_3 particles at 900 °C and 1200 °C. After 900 cycles the total crack length of the two materials is very close and shows a proportional increase. This shows that the thermal fatigue resistance of Mo-Al_2O_3 and Mo at 900 °C is about the same. The thermal fatigue crack morphology of the rolled Mo alloy at 1200 °C for different times is shown in Fig. 10. The Mo alloy plate after 200 cycles has a longer crack. The crack growth rate of the pure Mo plate increases significantly when the number of cycles reaches 400, and the crack begins to branch in Fig. 10(c). With a further increase in the number of cycles, the cracks in the pure Mo plate will continue to grow. When the number of cycles reaches 800, the length of the main crack will be close to the underwater depth of the sample, and the branched crack can be the main factor for subsequent crack propagation. Overall, when the number of cycles reaches 400, the crack growth rate of the pure Mo plate increases significantly, while the Mo alloy doped with Al_2O_3 has a smaller overall crack length. Compared with the total crack length after different number cycles, the total crack length of the Al_2O_3 composite Mo plate at 1200 °C is lower than that of the pure Mo plate. Therefore, the reduced in the design process of the crack initiation resistance is attributed to the ceramic particles Al_2O_3 enhancing the crack initiation resistance of the Mo alloy plates.

As described above, the ceramic particles Al_2O_3 can not only effectively control the grain size and distribution of Mo alloys, but also increase the yield strength of Mo alloys to 859 MPa. The quantitative yield strength model of Al_2O_3 particles related to annealing temperature is proved. The high temperature mechanical properties can be controlled by adding Al_2O_3 particles. Doped Al_2O_3 particles improve the hardness and strength of the Mo alloy by hydrothermal synthesis and pressureless sintering technology. This is because the fine Al_2O_3 particle size can play a joint role in grain strengthening and Orowan strengthening of Mo alloy. And the Mo alloy obtains from Al_2O_3 particles in PM process combined with pressureless sintering technology has excellent high-temperature compression properties and fatigue resistance. However, the current problems such as the lack of good ductility and high temperature strength of Mo-Al_2O_3 alloy have not been completely solved, which still limited the high temperature performance of Al_2O_3 particle reinforced Mo alloy materials [170].

2.4. Doped with ZrO_2 ceramic particles

For traditional ODS alloys, although oxides have the advantage of greatly inhibiting the growth of metal powders [171], they will hinder the densification process of the metal matrix. To explore oxides that can be used as both grain growth inhibitors and metal matrix sintering accelerators, there have been studies using HfO_2 as a sintering aid for W [172,173] and through theoretical calculations and experimental observations in Ref. [174], low-temperature accelerated sintering in the W-HfO_2 system has been explored to prepare high-density nanocrystalline alloys with excellent properties. However, there are few studies on accelerating powder sintering by doping oxide particles in Mo metal systems.

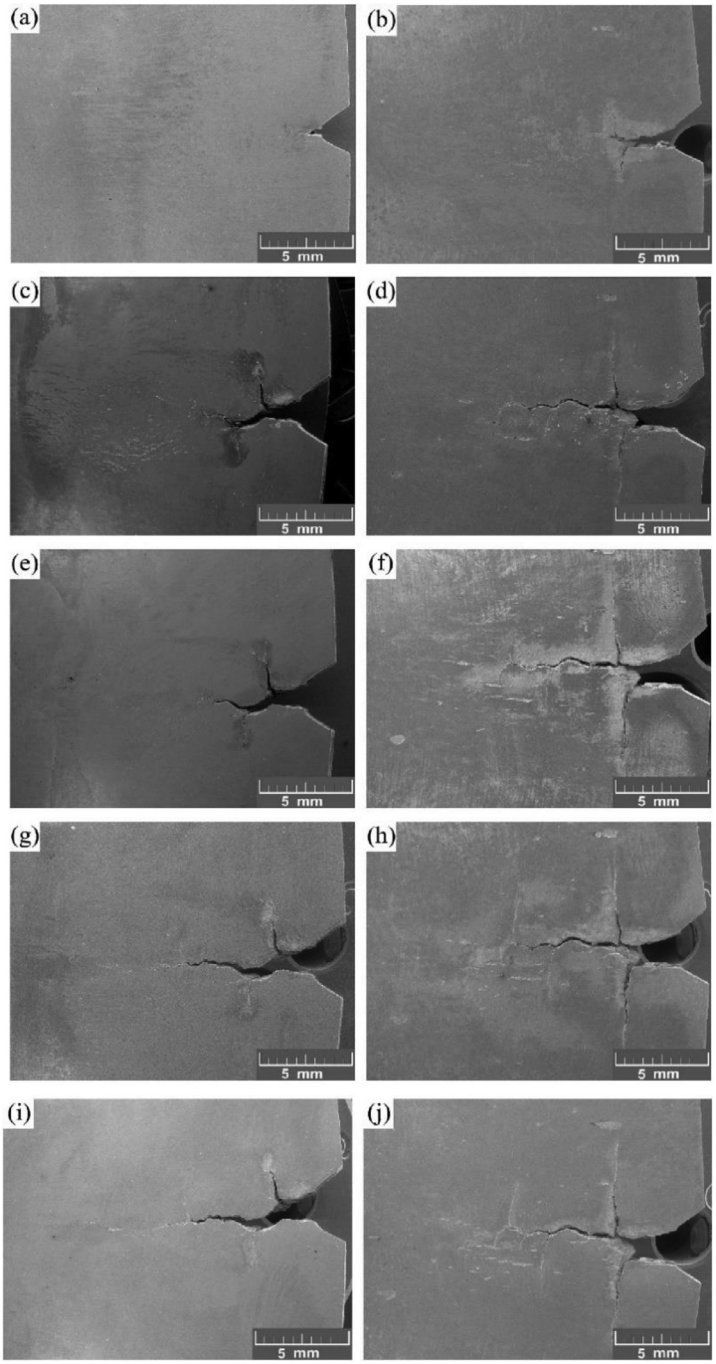

Fig. 10. Thermal fatigue crack morphology of rolled Mo plate after different numbers of cycles at 1200 °C: (a) Pure Mo, 200 cycles, (b) Mo-Al_2O_3, 200 cycles, (c) Pure Mo, 400 cycles, (d) Mo-Al_2O_3, 400 cycles, (e) Pure Mo, 600 cycles, (f) Mo- Al_2O_3, 600 cycles, (g) Pure Mo, 800 cycles, (h) Mo- Al_2O_3, 800 cycles, (i) Pure Mo, 1000 cycles, (j) Mo- Al_2O_3, 1000 cycles. Adapted with permission from Ref. [169]. Reprinted from Journal of Alloys and Compounds, 5411831257946, Copyright (2020), with permission from Elsevier.

In recent years, ZrO_2 particles have attracted more attention as ideal reinforcing particles for refractory the Mo alloys due to their stable chemical properties, high-temperature resistance, good high temperature and thermal conductivity [175–179]. In this section, we report the contribution of ZrO_2 particles as a sintering aid for Mo matrix and discussed the effects on the high-temperature and fatigue properties.

ZrO_2 ceramic particles can promote the sintering and densification process of the Mo matrix based on refining alloy powder. Dong et al. [180] noticed low-temperature accelerated sintering in Mo-ZrO_2 system and the effects of ZrO_2 ceramic particles on the properties of Mo alloys. First of all, they used a co-deposition wet chemical method to ensure that ZrO_2 was doped in the form of nanoparticles, and it was more favorable for the oxide to enter between the Mo particles, thereby forming nanocrystalline grains. Then the isothermal densification evolution was analyzed for pure Mo powder and Mo-ZrO_2 powder at sintering temperatures of 1100 °C, 1300 °C, and 1480 °C, as seen in Fig. 11(a) and (b). The relative density of pure Mo powder sintered at 1300 °C increases to 0.88, its grain size increases from 0.45 μm to 0.92 μm, and the relative density of Mo-ZrO_2 increases to 0.85, which shows that ZrO_2 particles promote the densification behavior of the Mo matrix to a certain extent. The isothermal densification behavior of the two powders is analyzed in depth, and the idealized shrink-

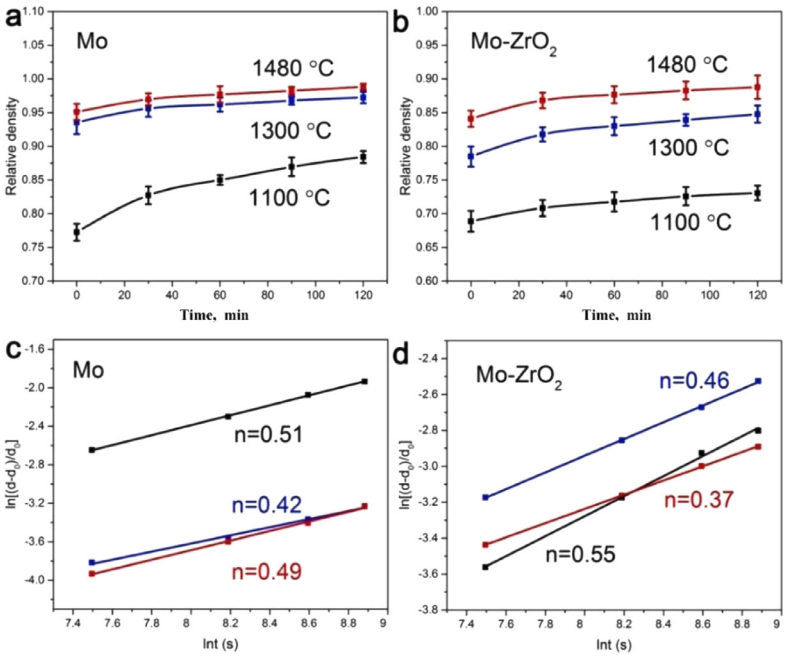

Fig. 11. Relative density vs. time curves during the isothermal sintering process at different temperatures: (a) pure Mo powder and (b) Mo-ZrO_2 powder. Logarithmic plots at different temperatures for (c) pure Mo powder and (d) Mo-ZrO_2 powder. Adapted with permission from Ref. [180]. Reprinted from Journal of Alloys and Compounds, 5,411,841,129,285, Copyright (2022), with permission from Elsevier.

age equation is used to simulate the isothermal sintering of the two powders. Since the compact shows isotropic shrinkage behavior after sintering, the corresponding equation can be written as:

$$\left(\frac{\Delta L}{L_0}\right) = \frac{1}{3}\frac{\Delta V}{V_0} = \frac{1}{3}\left(\frac{d-d_0}{d_0}\right) = kt^n \tag{16}$$

Here, L is the shrinkage length of the sample at time t, L_0 is the length of the sample at t_0, d_0, d, and V are the initial and final density and volume of the sintered sample, respctively. k is the Boltzmann constant, t is the absolute temperature, and n is an exponent to determine the main diffusion mechanism of densification. The calculated value of n can be used to predict the main diffusion mechanism during sintering. Eq. (16) can be expressed in the logarithmic form as

$$\ln\left(\frac{d-d_0}{d_0}\right) = n\ln t + \ln k \tag{17}$$

Fig. 11(c) and (d>) show the logarithmic plots and slope n values for pure Mo and Mo-ZrO_2 powders. The main mechanism of the sintering process of pure Mo is bulk diffusion [1], and the n of the Mo-ZrO_2 system varies from 0.46 to 0.37, indicating that grain boundary diffusion has a greater effect on densification than bulk diffusion. The ZrO_2 particles can enhance Mo matrix grain boundary diffusion and contribute to densification in PM sintering. Coupled with the high thermal stability of the ZrO_2 particles, the forged Mo-ZrO_2 alloy has stable high strength at high temperatures.

The ZrO_2 ceramic oxide addition also can increase the high-temperature mechanical properties of Mo alloys [181]. Xu et al. [182] paid special attention to the effects of ZrO_2 on the compression properties and thermal deformation behavior of Mo alloys. They prepared Mo-ZrO_2 composite powder by hydrothermal synthesis, coprecipitation, and co-decomposition methods [62], and then through cold isostatic pressing (280 MPa, 15 min) and pressureless sintering (1920 °C, 3 h), they obtained Mo alloy rods with different nanoscale ZrO_2 content (0–2 vol.%). The compression properties and hot deformation behavior are tested at different temperatures and strain rates. According to the true stress–strain curve of the Mo alloy with different ZrO_2 contents during compression, as well as room temperature and high temperature ranging from 1000 °C to 1400 °C, it can be concluded that CYS is affected by ZrO_2 content and processing state. Compared with pure Mo, the CYS is increased by 18.9% and 65.6% at 1200 °C, respectively. When the temperature increases to 1400 °C and the ZrO_2 content increases to 2 vol.%, the CYS is significantly improved, indicating that a higher test temperature can significantly improve the high-temperature mechanical properties of the Mo alloy. By comparing the peak flow stress under high-temperature compression [183], it is found that the higher peak flow stress at the same strain rate is obtained for the Mo-2 vol.% ZrO_2 alloy. Thus, such good high-temperature compression properties are derived from the formation of ultrafine ZrO_2 particles in Mo alloy. The high-temperature strengthening effect of ultrafine ZrO_2 particles is also analyzed in Ref. [184]:

$$\mu = (S_1 - S_2)/S_1 \tag{18}$$

Here, μ is the strengthening effect of ZrO_2, S_1 and S_2 are the maximum stress values of the alloy and pure Mo, respectively. The strengthening effect increases significantly with temperature. Doping ZrO_2 particles can effectively prevent dislocation and crack propagation, refined grains, and reduced the possibility of cracks. This pinning effect delays its recrystallization behavior [185–187], thereby enhancing the high-temperature deformation resistance of Mo alloys [188]. Therefore, the excellent high-temperature mechanical properties of Mo-ZrO_2 alloy will guide future research of superalloys.

Fatigue failure is a common failure mode of the Mo alloy [189], which is the most harmful to Mo alloy [190]. There are few studies on the fatigue properties of ODS Mo alloys, and some literature reports have studied the fatigue properties of La_2O_3 and Al_2O_3 particle dispersion-strengthened Mo alloys [97,169]. The low cycle fatigue (LCF) and fatigue absorption energy of ZrO_2 dispersion strengthened Mo alloy has been reported in [191]. Comparing the variations of peak tensile stress versus the number of cycles for Mo in Fig. 12, it is shown that the stress peak value of Mo-0.5%

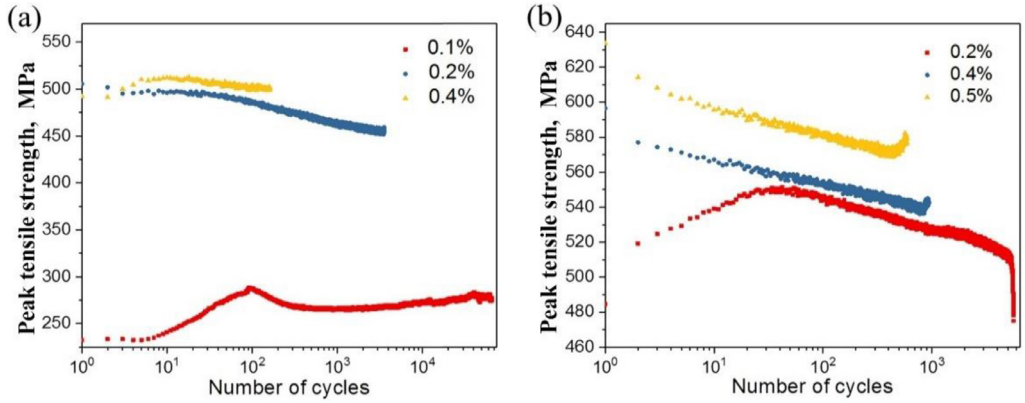

Fig. 12. Variations of peak tensile stress versus the number of cycles for (a) Mo, (b) Mo-0.5%ZrO_2. Adapted with permission from Ref. [191]. Reprinted from Journal of Alloys and Compounds, 5411850614486, Copyright (2021), with permission from Elsevier.

ZrO_2 is higher than pure Mo under the same strain amplitude. Similarly, the energy absorption capacity of the Mo alloy is improved by adding ZrO_2, which makes the fatigue life of Mo-0.5% ZrO_2 higher than pure Mo in Fig. A.6 in Supplementary Materials. In fact, the cyclic deformation is strongly related to the magnitude of the strain and the microstructure. For pure Mo and Mo-0.5% ZrO_2 recrystallized after annealing at 1050 °C, the intragranular ZrO_2 would strongly hinder dislocations and inhibit grain boundary movement, which causes Mo-1.5% ZrO_2 to had a higher initial dislocation density. When the initial dislocation density is relatively high, the dislocation rearrangement or annihilation rate can be accelerated by cyclic plastic deformation, resulting in the occurrence of cyclic softening of the Mo-0.5% ZrO_2 alloy. The addition of ZrO_2 particles not only kept the yield stage longer but cyclic softening only occurred in higher strain amplitudes. Then Xu et al. [192] further prepared Mo alloys containing 1.2% and 2.0% ZrO_2 by using the liquid-liquid doping method of ZrO_2 doped Mo alloys. It is proved that 1.2% ZrO_2 has the strongest fatigue performance, and the peak stress increased with the increase of strain amplitude. The Mo-1.2% ZrO_2 alloy has good fatigue life. In summary, ZrO_2 particles can increase the total fatigue absorption energy of Mo alloys under the same strain amplitude and improve the fatigue properties of Mo alloys.

So the ZrO_2 ceramic particles can prepare by wet chemical method, hydrothermal synthesis technology and pressureless sintering technology not only promotes the grain boundary diffusion and grain refinement of the Mo matrix, but contributes to sintering densification and hindering the movement of dislocations to the GBs. Doped ZrO_2 particles make cyclic softening not easy to occur, prolongs fatigue life, significantly improves the plastic deformation ability and high-temperature strengthening effect of Mo alloy. The ZrO_2 particles with controllable composition, nanometer size, uniform distribution and appropriate content are the key to strengthening Mo alloy. As a sintering aid, ZrO_2 particles have strong dispersion strengthening and dislocation pinning effect on the alloy, which will be used to prepare other ultra-fine dense alloy systems.

3. Carbide precipitation-strengthened design

As compared with the oxide dispersion-strengthened phases, some carbides with ultra-high melting point are also widely used as strengthening materials for Mo alloys. Carbides are widely used in Mo alloys because of their good mechanical properties, high melting point, hardness, and good thermal stability. Carbide particles can also effectively inhibit the grain growth and grain boundary migration of the Mo matrix. These alloys mainly rely on the addition of TiC, ZrC, NbC, HfC [193] particles, and other carbide particles to achieve a uniform grain structure and excellent high-temperature strength and toughness. The addition of refractory TiC and ZrC particles can significantly strengthen the properties of Mo alloys, which are promising candidates for ultra-high-temperature materials other than nickel-based high temperature alloys.

3.1. Refractory TiC particles addition

Unlike oxide-dispersed Mo alloys, the uneven distribution of carbides results in large particles during sintering [194,195]. The developed freeze-drying method already offers the possibility to improve the grain refinement and sintering densification of Mo-TiC alloys [196]. Hu et al. [197] fabricated a new freeze-drying technology with polyvinylpyrrolidone (PVP) and polyethyleneglycol (PEG) polymer dispersant to mix TiC particles with Mo powder, and obtained Mo powder with a grain size of 95 nm and one-third of the original pure Mo sizes. The Mo grain is refined from 8.9 μm to 2.4 μm in the corresponding low-temperature sintering process. HR-TEM analysis shows that the TiC particles are able to maintain their particle size and did not grow into larges particles. The most carbide particles are mainly TiC phase in Fig. 13(a–d), and a few were Ti_8C_5 or TiO_2 phases in Fig. 13(e) and (f). According to the crystal spacing of TiC (0.216 nm (2 0 0), 0.153 nm (2 2 0), 0.125 nm (2 2 2)), Ti_8C_5 (0.216 nm (0 2 4), 0.153 nm (2 2 0), 0.152 nm (2 0 8)) and TiO_2 (0.218 nm (1 1 1), 0.162 nm (2 2 0)), the crystal spacing of Mo matches well, so it is easier to form stable coherent Mo/carbide interface. The growth of Mo and carbide is effectively hindered so that Mo and carbide are ultrafine in size, and the ultrafine grain structure has high hardness and strength. Therefore, adding TiC particles can effectively refine and obtain high-density Mo alloys [198]. Similarly, Tuzemen et al. [199] produced TZM-TiC and TZM-ZrC composites by SPS. Not only TiC and ZrC can be uniformly distributed in the Mo matrix, but also the carbide content can refine the grain size, increasing the hardness value of TZM-TiC composites. The TZM-TiC composites have higher hardness than TZM-ZrC composites, and the highest hardness value increases to 4.1 GPa. TiC/Mo-based composites are synthesized for the first time by in-situ laser powder bed fusion (PBF) of carbon nanotubes (CNTs) [200]. In this way, TiC reinforcements can also be uniformly dispersed to obtain fine equiaxed grains. The average grain size decreases from 14.2 μm to 3.3 μm, and the Vickers hardness is significantly improved after adding TiC. Therefore, the addition of TiC provides a valuable reference for designing the PBF process to fabricate advanced Mo-based composites.

Recently, the mechanical properties and high-temperature mechanical properties of Mo alloys with TiC particles have been dis-

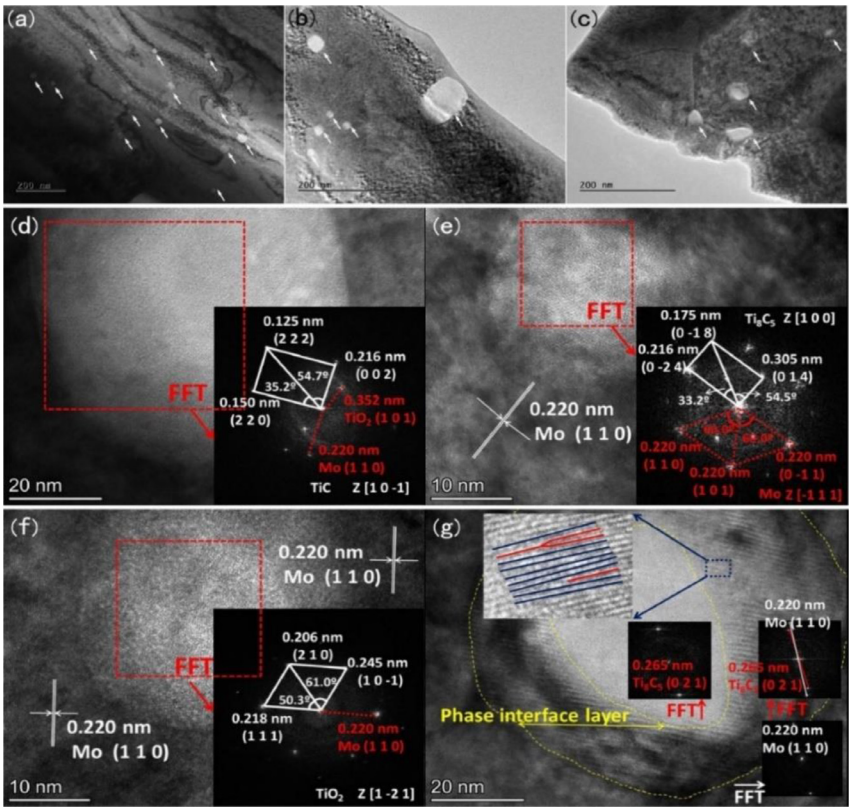

Fig. 13. (a)–(c) TEM images of freeze-dried Mo-TiC alloys, (d)–(g) HRTEM images of freeze-dried Mo-TiC alloys. Adapted with permission from Ref. [197]. Reprinted from Scripta Materialia, 5411851048789, Copyright (2021), with permission from Elsevier.

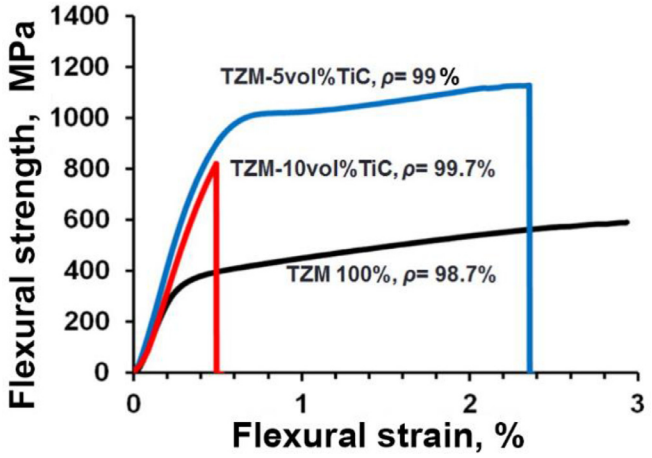

Fig. 14. Flexural stress–strain curves for TZM, TZM-5 vol.%TiC, and TZM-10 vol.% TiC sintered at 2000 °C, 35 MPa, 15 min. Arrow indicates TZM 100% ductility extended beyond the range of the bend testing fixture. Adapted with permission from Ref. [206]. Reprinted from International Journal of Refractory Metals and Hard Materials, 5411851383082, Copyright (2017), with permission from Elsevier.

cussed and explored [201–205]. Browning et al. [206] analyzed the sintered density, hardness, and flexural strength of Mo-TiC alloys. The hardness of Mo-10 wt.% TiC alloy obtained by the field-assisted sintering technique (FAST) is higher than pure TZM alloy. The TZM-5 vol.% TiC alloy has the highest bending strength of 1144±181 MPa and higher flexural elongation at failure in Fig. 14. The flexural strength of the TZM-10 vol% TiC sample slightly decreases to 925±109 MPa, which is still higher than the strength of pure TZM material of 617.2±50.9 MPa. Zhao et al. [207] debated the TiC addition effects on the bonding properties and fracture toughness of Mo through first-principles calculations. It is demonstrated that the interfacial orientation led to the different effects of TiC particles on Mo toughness and ductility. TiC particles improve the toughness of the Mo (1 1 0) surface but at the same time decrease the cohesive strength of Mo (1 0 0) and (1 1 0) surfaces. The electronic structure of Mo became nonlocal, which intrinsically increases the fracture toughness/ductility of the Mo (1 1 0) surface. Thus, the fracture toughness of Mo (1 0 0)-TiC (1 0 0) interface (2.740 MPa $m^{1/2}$) is much smaller than that of Mo (1 0 0) surface (3.318 MPa $m^{1/2}$), and the K_{IC}^{hkl} (2.099 MPa $m^{1/2}$) value of Mo (1 1 0)-TiC (1 0 0) interface is also lower than that of pure Mo (1 1 0) interface (2.581 MPa $m^{1/2}$). In a word, the interface orientation of TiC has different contributions to the fracture toughness of Mo (1 0 0) or Mo (1 1 0) surface. The influence of different temperatures on the interface strength, fracture toughness and high-temperature strength of Mo-TiC can be further studied.

Freeze-drying technology provides the possibility to prepare ultrafine and uniformly dispersed TiC particles. In contrast to freeze-drying method (Mo alloy grain refinement to 2.4 μm), laser powder bed fusion method has fine Mo equiaxial grains (3.3 μm), superior hardness and strength. From the mechanical alloying method combined with SPS sintering technology, TiC particles as reinforcement reduce the grain growth of Mo alloy and have the highest hardness value (4.1 GPa) and excellent bending strength (1144 ± 181 MPa).

3.2. Refractory ZrC particles addition

Nano-sized ZrC particles show obvious advantages in Mo strengthening [208,209]. Jing et al. [210] designed the Mo alloy with high strength, good ductility, and thermal stability through nanoscale ZrC particles precipitation and interface control. ZrC precipitation-strengthened Mo alloy rods with an average grain

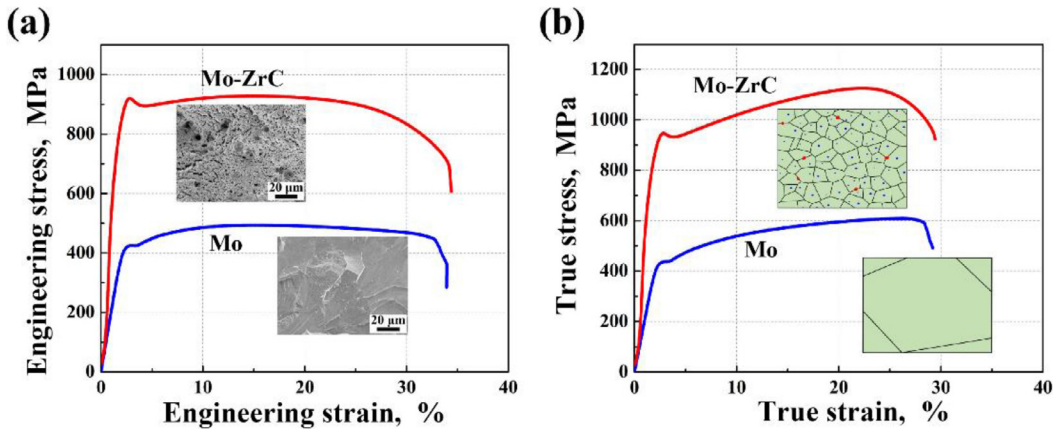

Fig. 15. (a) Engineering and (b) true stress–strain curves of pure Mo and Mo-ZrC alloy at room temperature. Insets in Fig. 1(a) are the corresponding SEM micrographs of fracture surfaces. Insets in Fig. 1(b) show the schematic microstructure of pure Mo and Mo-ZrC. Adapted with permission from Ref. [210]. Reprinted from Acta Mater.ialia, 5411860254205, Copyright (2022), with permission from Elsevier.

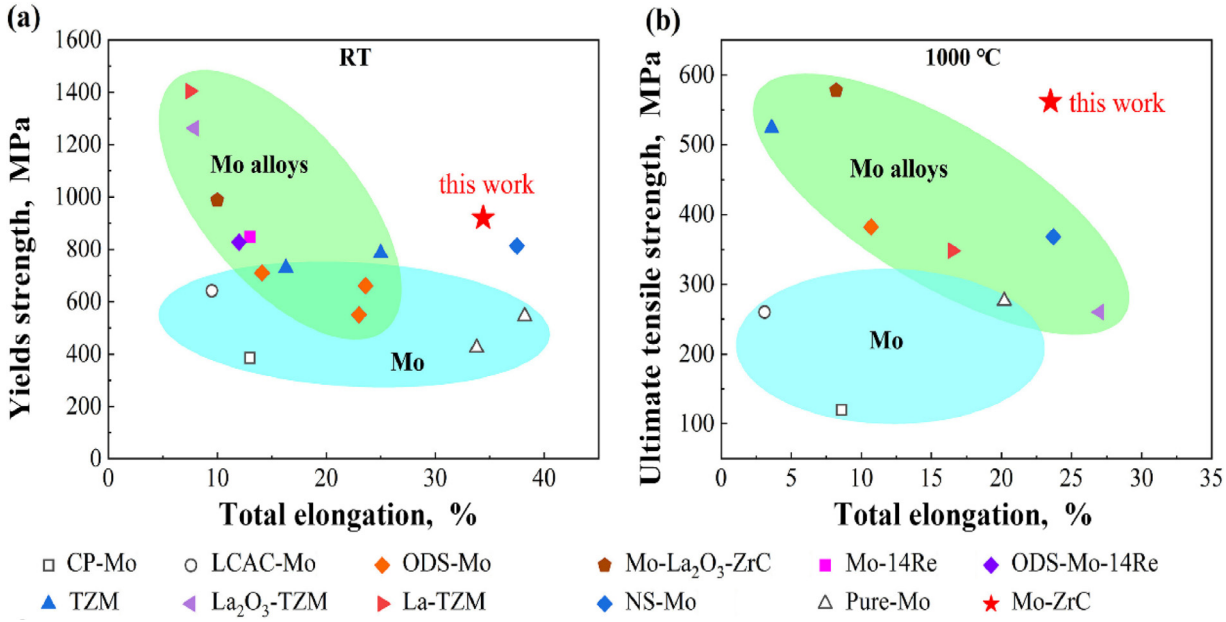

Fig. 16. (a) Yield strength and total elongation of Mo-ZrC alloy at room temperature, and (b) tensile strength and total elongation of Mo-ZrC alloy at 1000 °C. Also included are data from some other Mo materials in the literature. Adapted with permission from Ref. [210]. Reprinted from Acta Materialia, 5411860254205, Copyright (2022), with permission from Elsevier. (CP-Mo [68], NS-Mo [68], ODS-Mo [38,68,104], Mo-14Re [57], ODS-Mo-14Re [57], LCAC-Mo [38,68], TEM [38,68], Mo-La_2O_3-ZrC [215], La-TZM [99]).

size of only 0.67 μm are prepared by powder ball milling, cold isostatic pressing, high-temperature sintering, rotary forging, and annealing. Comparing the tensile engineering stress-strain curves of Mo and Mo-ZrC alloys at room temperature in Fig. 15, the yield strength (YS) and ultimate tensile strength (UTS) of Mo-ZrC alloy are doubled compared with pure Mo. The yield strength, total elongation, and ultimate tensile strength of Mo-ZrC alloy are compared with Mo metal reported in the literature in Fig. 16. It is found that the YS of Mo-ZrC alloy at room temperature (920 MPa) is about 26% higher than the TZM alloy (730 MPa), and the elongation of Mo-ZrC (34.4%) is twice higher than TZM [130]. The UTS of Mo-ZrC alloy is significantly higher than pure Mo, and it still maintained good ductility, indicating that the addition of ZrC particles shows outstanding mechanical properties at high temperatures. The thermal stability of Mo-ZrC alloy is also evaluated up to 1400 °C, which was much higher than $0.4T_m$. The recrystallization starting temperature of pure Mo metal is about $0.4T_m$ (T_m = 2896 K), indicating that it has excellent high temperature stability [211], which is the main reason for maintaining good mechanical properties at high temperature. The uniformly distributed ZrC nanoparticles causes an ultra-fine grain structure of the Mo alloys. First-principles calculations has shown in Ref. [212] that the doped ZrC particles are able to obtain stronger Mo-C bonds and weaker Mo-O bonds in the Mo alloy, thereby controlling their interface. Moreover, the fracture toughness of ZrC particles in Mo alloy at room temperature had also been reported [213]. It was proved in Ref. [214] that ZrC particles played an effective role in the toughening of Mo alloy. They systematically analyzed the impact of adding ZrC on the fracture toughness of Mo-Si-B alloy at room temperature, and obtained that the average fracture toughness of Mo-Si-B alloy with different compositions was between 12.4 and 20.3 MPa $m^{1/2}$, proving the synergistic toughening effect of ZrC particles.

Excellent high-temperature mechanical properties and high recrystallization temperature are essential in industrial applications. The addition of ZrC particles can further improve the high temperature mechanical properties of Mo alloys [216]. The Mo-0.8% La_2O_3–2% ZrC alloy is prepared by adding ZrC nanoparticles by

traditional PM technology [215]. It has a high tensile strength of 988 MPa and 189 MPa at room temperature and 1400 °C, respectively. They explained the important strengthening effects of ZrC and La_2O_3 grains dislocation strengthening, grain refinement strengthening, and secondary-phase grain strengthening on Mo alloys by the Taylor relation, Hall-Petch, and Orowan-Ashby mechanisms. Therefore, ZrC particles play a key role in strengthening the alloy, effectively improving the recrystallization temperature and high-temperature performance of the Mo alloy.

In current Mo alloys, the carbide particle size is relatively large (even in the 20–150 nm nanometer sizes). If the carbide phase particles can be refined to 10 nm or less, the mechanical properties and high-temperature mechanical properties might be further improved by the synergistic effect of particle precipitation strengthening, fine grain strengthening and grain boundary strengthening. By using mechanical alloying and pressureless sintering technology, the grain size of Mo alloy is about 0.67 μm, and the yield strength and tensile strength have been increased. Therefore, for ZrC particles, the effect of strengthening Mo alloy has been achieved by using PM process. It is reduced the production cost of the process, and it is conducive to further exploring and designing the new development direction of high-strength and toughness Mo alloy industry.

4. Summary and outlook

Designing Mo alloys by doping metal oxides and carbides is a simple, convenient and effective method, which results in the high strength, toughness, and high-temperature resistance of Mo alloys. Many fundamental studies have confirmed that high-performance Mo alloys have great potential as materials for industrial applications and production based on the strengthening of metal oxides and carbides. In this paper, the influence of metal oxide/carbide doping on the microstructure and properties of Mo alloy is reviewed. We attempt to shed light on the strengthening mechanism, the recent advances and the future status of Mo alloys doped with different metal oxides/carbides. The following points can be summarized:

(1) The geometric characteristics of metal oxides/carbides, such as particle morphology, particle size, distribution and volume fraction, are the key factors affecting the microstructure and properties of Mo alloys. The design and production of Mo alloy products doped with metal oxides and carbides have attracted more and more research interests. To obtain metal oxides/carbides with high sintering activity, nanometer particle size, uniform distribution and suitable volume fraction, the research methods has changed from mechanical alloying and conventional sintering methods with metal oxides/carbides to improved hydrothermal synthesis, freeze-drying and co-precipitation chemical deposition. Using different doping technologies to doping metal oxides/carbides, the designed Mo alloy has played a crucial role in excellent hardness, yield strength, compressive strength and fracture toughness, high-temperature mechanical properties, oxidation resistance and other aspects. The Mo alloy designed by doping metal oxides/carbides with different doping technologies plays a crucial role in hardness, yield strength, compressive strength and fracture toughness, high-temperature mechanical properties, oxidation resistance, etc. Most importantly, this work will also attract those who want to design better materials for other refractory metal materials. They hope to cooperate with multi-technology optimization in the metal oxide and carbide doping methods of the target materials to develop the next generation of high-performance material design.

(2) Comparing the effect of different preparation technologies on strengthening Mo alloy, it is found that doping metal oxide La_2O_3 particles, Y_2O_3 particles and refractory TiC particles by freeze drying technology can make Mo alloy reach a significant balance between ultrafine particles and relative density. Nano-sized La_2O_3 particles (<5 nm) are created and the Mo grains was refined to 440 nm with high hardness (495 $HV_{0.2}$), and strength (1201 MPa) at 30% strain. The 54 nm mixed powder, 620 nm finest grain size and high density (99.6%) Mo alloy are obtained by doping Y_2O_3 particles. At the same time, Mo alloy has high hardness of 487 ± 28 $HV_{0.2}$, high yield strength of 902 MPa and high compressive strength of 1110 MPa. For TiC particles, the freeze-drying technology prepared Mo powder with a particle size of 95 nm and refined the grain size to 2.4 μm. It can able to deeply understand the effect of metal oxide/carbide prepared by freeze-drying technology on the microstructure and comprehensive properties of Mo alloy. It is beneficial to further refine the nanoparticles and effectively improve the dispersion strengthening and precipitation strengthening effect of Mo matrix, so that Mo alloy has a good development prospect in the field of high-temperature applications.

(3) Hydrothermal synthesis technology and mechanical alloying combined with pressureless sintering and spark plasma sintering are of great significance in the design of Mo alloys strengthened via doping metal oxide/carbide. Hydrothermal synthesis has been widely used in the preparation of doped oxide particle in Mo alloys. It will greatly promote the uniform distribution of the particles into the Mo, making the mixed powder refined to 3.9 μm. The tensile strength and the maximum yield strength of Mo-Y_2O_3 alloy reaches 917 MPa and 859 MPa, respectively. The compression strength of Mo-ZrO_2 alloy at high temperature is 65.6% higher than that of pure Mo, which has a prominent strengthening effect at high temperature. Mechanical alloying combined with pressureless sintering technology is commonly used in metal oxide/carbide strengthened Mo alloys. Among them, doped with refractory ZrC particles, the grain size can be designed to be 670 nm and room temperature yield strength is about 920 MPa in Mo alloy. It can reduce the production process cost and promote the exploration and design new development direction of high-performance Mo alloy industry. In addition, the hardness (4.10 GPa) and bending strength (1144±181 MPa) of TiC particles prepared by spark plasma sintering (SPS) and mechanical alloying are improved. Therefore, the hydrothermal synthesis, mechanical alloying, pressureless sintering and spark plasma sintering (SPS) technology can achieve dispersed/precipitated particles with controllable doping composition, nanometer size, uniform distribution and appropriate content, which will become the key to strengthening Mo alloy.

The following lists some limitations and some future research directions in this field:

(1) Improving the ductility and high-temperature strength of Mo alloys is the key to developing advanced Mo alloys. Research on designing high-performance Mo alloys has focused on the addition of metal oxides with La_2O_3, Al_2O_3, ZrO_2 and Y_2O_3 particles as well as metal carbide TiC and ZrC particles, while the mechanical properties of other metal oxides such as cerium oxide (CeO_2), metal carbides NbC, HfC and their relationship with microstructure characteristics and strengthening mechanisms has been rarely reported. In particular, the high-temperature mechanical properties have been inadequately studied. It is important to further study and determine the effects of different metal oxides and carbides on the microstructure changes and strengthening mechanisms of Mo alloys.

(2) In order to obtain uniformly dispersed and fine-grained oxide and carbide addition, which can refine the grain of the Mo matrix and prevent dislocation slip, new methods have been proposed to design high-performance Mo alloys, including freeze-drying methods to obtain Mo-Y_2O_3 and Mo-La_2O_3 alloys with compressive strengths of 1110 MPa and 1201 MPa, respectively, the compressive yield strength of 644.5 MPa are obtained by co-precipitation and low-temperature sintering, and the addition of ZrO_2 to Mo alloys as a general new method for accelerated sin-

tering can also be applied to other systems for preparing ultra-fine dense Mo alloys. It has greatly improved the comprehensive performance of Mo alloys. Therefore, these methods will be a key role for the preparation of ODS-Mo alloys in the future and have a certain guiding significance for industrial production.

(3) In the current application and development of Mo alloys, although the size of added oxides and carbides can reach the nanoscale (even in the size of 20–150 nm), the uniformity of dispersed particles and high-temperature stability need to be improved. Further refinement of nano particles can effectively improve the dispersion and precipitation strengthening effect in Mo matrix, which makes Mo alloys have a good development prospect in the field of high-temperature applications.

To design and manufacture high-performance Mo alloy materials, it is necessary to consider and explore the particle types, methods, technologies and particle size shapes of doped oxides and carbides, as well as the application fields of high-performance Mo alloys. Although recent great breakthroughs in performance achieved, research related to preparation techniques and the manufacture of high-performance Mo alloys is still in the beginning stages. At the same time, it is hoped that advanced Mo alloy materials with different particles of metal oxides and carbides will become more and more useful. Hopefully, this review can further stimulate and guide interest in the study of Mo-based composites, and we look forward to more robust applications on advanced materials at high temperature in issues involving doped metal oxides and carbide strengthening alloys. Furthermore, the nanocomposites with special properties (physical, chemical, mechanical, electrical, magnetic and optical) may be expected to investigate, which cannot be achieved by conventional processes and preparation methods.

Declaration of Competing Interest

The authors declare that they have no known competing financial interests or personal relationships that could have appeared to influence the work reported in this paper.

CRediT authorship contribution statement

Hairui Xing: Writing – original draft, Writing – review & editing. **Ping Hu:** Supervision, Project administration. **Chaojun He:** Software. **Xiangyang Zhang:** Validation. **Jiayu Han:** Investigation. **Fan Yang:** Methodology. **Run Bai:** Data curation. **Wen Zhang:** Resources. **Kuaishe Wang:** Funding acquisition. **Alex A. Volinsky:** Visualization.

Acknowledgments

This work was supported by the Outstanding Doctorate Dissertation Cultivation Fund of Xi'an University of Architecture and Technology (No. 160842012), Scientific and Technological Innovation Team Project of the Shaanxi Innovation Capability Support Plan, China (No. 2022TD-30), the Fok Ying Tung Education Foundation (No. 171101), Youth Innovation Team of Shaanxi Universities (No. 2019-2022), Top young talents project of "Special support program for high-level talents" in the Shaanxi Province (No. 2018-2023), Major scientific and technological projects in the Shaanxi Province of China (No. 2020ZDZX04-02–01), Service local special program of education department of Shaanxi province, China (No. 21JC016), General Special Scientific Research Program of the Shaanxi Provincial Department of Education (No. 21JK0722), the General Projects of Key R&D Program of the Shaanxi Province, China (No. 2021GY-209), China Postdoctoral Science Foundation (No. 2021M693878) and China Postdoctoral Science Foundation (No. 2021MD703866).

Data availability

No.

Supplementary materials

Supplementary material associated with this article can be found, in the online version, at doi:10.1016/j.jmst.2023.03.026.

References

[1] S. Majumdar, S. Raveendra, I. Samajdar, P. Bhargava, I.G. Sharma, Acta Mater. 57 (2009) 4158–4168.
[2] S.J. Wang, H. Wang, K. Du, W. Zhang, M.L. Sui, S.X. Mao, Nat. Commun. 5 (2014) 3433.
[3] S. Primig, H. Clemens, W. Knabl, A. Lorich, R. Stickler, Int. J. Refract. Met. Hard Mater. 48 (2015) 179–186.
[4] J.H. Perepezko, Science 326 (2009) 1068–1069.
[5] D.M. Dimiduk, J.H. Perepezko, MRS Bull. 28 (2003) 639–645.
[6] M. Higashi, T. Ozaki, Mater. Des. 191 (2020) 108588.
[7] Y.H. Yoon, S.Y. Lee, J.G. Gwon, H.J. Cho, Q. Wu, Y.H. Kim, W.H. Lee, Ceram. Int. 44 (2018) 16647–16653.
[8] İ.A. Kariper, F.M. Tezel, Ceram. Int. 45 (2019) 3478–3482.
[9] B.V. Cockeram, T.S. Byun, K.J. Leonard, J.L. Hollenbeck, L.L. Snead, J. Nucl. Mater. 440 (2013) 382–413.
[10] B. Tabernig, N. Reheis, Int. J. Refract. Met. Hard Mater. 28 (2010) 728–733.
[11] S.T. Mileiko, Ceram. Int. 45 (2019) 9439–9443.
[12] B. Meng, M.W. Fu, M. Wan, J. Adv. Manuf. Technol. 78 (2015) 1005–1014.
[13] S.P. Chakraborty, S. Banerjee, I.G. Sharma, A.K. Suri, J. Nucl. Mater. 403 (2010) 152–159.
[14] X.B. Zhao, Z.H. Ye, Surf. Coat. Technol. 228 (2013) S266–S270.
[15] H.R. Xing, P. Hu, S.L. Li, Y.G. Zuo, J.Y. Han, X.J. Hua, K.S. Wang, F. Yang, P.F. Feng, T. Chang, J. Mater. Sci. Technol. 62 (2021) 180–194.
[16] I. Wesemann, A. Hoffmann, T. Mrotzek, U. Martin, Int. J. Refract. Met. Hard Mater. 28 (2010) 709–715.
[17] S. Primig, H. Leitner, H. Clemens, A. Lorich, W. Knabl, R. Stickler, Int. J. Refract. Met. Hard Mater. 28 (2010) 703–708.
[18] S. Majumdar, R. Kapoor, S. Raveendra, H. Sinha, I. Samajdar, P. Bhargava, J.K. Chakravartty, I.G. Sharma, A.K. Suri, J. Nucl. Mater. 385 (2009) 545–551.
[19] B. Dubiel, M. Chmielewski, T. Moskalewicz, A. Gruszczyński, A. Czyrska-Filemonowicz, Mater. Lett. 124 (2014) 137–140.
[20] C. Pöhl, J. Schatte, H. Leitner, J. Alloy. Compd. 576 (2013) 250–256.
[21] B.V. Cockeram, R.W. Smith, N. Hashimoto, L.L. Snead, J. Nucl. Mater. 418 (2011) 121–136.
[22] H.R. Xing, P. Hu, J.Y. Han, S.L. Li, S.W. Ge, X.J. Hua, B.L. Hu, F. Yang, K.S. Wang, P.F. Feng, Int. J. Refract. Met. Hard Mater. 103 (2022) 105747.
[23] M.K. Miller, E.A. Kenik, M.S. Mousa, K.F. Russell, A.J. Bryhan, Scr. Mater. 46 (2002) 299–303.
[24] N.P. Daphalapurkar, S. Patil, T. Nguyen, K.E. Prasad, K.T. Ramesh, Mater. Sci. Eng. A 738 (2018) 283–294.
[25] N. Tutyshkin, W.H. Müller, R. Wille, M. Zapara, Int. J. Plast. 59 (2014) 133–151.
[26] B.H. Duan, Z. Zhang, D.Z. Wang, T. Zhou, Trans. Nonferr. Metal. Soc. 29 (2019) 1705–1713.
[27] C.B. Danisman, B. Yavas, O. Yucel, F. Sahin, G. Goller, J. Alloy. Compd. 685 (2016) 860–868.
[28] X.J. Yu, K.S. Kumar, Mater. Sci. Eng. A 676 (2016) 312–323.
[29] Y. Wang, J.C. Gao, G.M. Chen, W.Q. Li, Y.G. Zhou, W. Zhang, Int. J. Refract. Met. Hard Mater. 26 (2008) 9–13.
[30] S.P. Chakraborty, S. Banerjee, I.G. Sharma, B. Paul, A.K. Suri, J. Alloy. Compd. 477 (2009) 256–261.
[31] G. Leichtfried, J.H. Schneibel, M. Heilmaier, Metall. Mater. Trans. A 37 (2006) 2955–2961.
[32] H. Sıralı, D. Şimşek, D. Özyürek, Met. Mater. Int. 27 (2021) 4110–4119.
[33] M. Aziz, D.C. Hudson, S. Russo, Appl. Phys. Lett. 104 (2014) 233102.
[34] C.P. Cui, Y.M. Gao, S.Z. Wei, G.S. Zhang, Y.C. Zhou, K.M. Pan, X.W. Zhu, S.L. Guo, High Temp. Mater. Process. 36 (2017) 167–173.
[35] P. Hu, Y.G. Zuo, S.L. Li, H.R. Xing, J.Y. Han, S.W. Ge, X.J. Hua, K.S. Wang, W. Zhang, J.B. Fu, J. Alloy. Compd. 870 (2021) 159429.
[36] M.S. El Genk, J.M. Tournier, J. Nucl. Mater. 340 (2005) 93–112.
[37] E. Ahmadi, M. Malekzadeh, S.K. Sadrnezhaad, Int. J. Refract. Met. Hard Mater. 29 (2011) 141–145.
[38] B.V. Cockeram, Mater. Sci. Eng. A 418 (2006) 120–136.
[39] C. Chen, S. Wang, Y.L. Jia, M.P. Wang, Z. Li, Z.X. Wang, J. Alloy. Compd. 589 (2014) 531–538.
[40] S.W. Jin, L.Z. Mei, Y.M. Shu, Y.Z. Tie, J. Alloy. Compd. 419 (2006) 172–175.
[41] L. Zhang, M. Zhang, Z. Zhu, M. Gao, J. Gao, Z. Guo, J. Alloy. Compd. 918 (2022) 165571.
[42] L.A. Díáz, A.F. Valdés, C. Dıáz, A.M. Espino, R. Torrecillas, J. Eur. Ceram. Soc. 23 (2003) 2829–2834.
[43] M. Nawa, T. Sekino, K. Niihara, J. Mater. Sci. 29 (1994) 3185–3192.
[44] K.Q. Liu, W. Pan, Z.K. Fan, H.J. Zhang, R.J. Shi, S.J. Yin, Y.P. Ren, Rare Metal. Mater. Eng. 36 (2007) 238–240.
[45] Z.N. Xu, L.J. Xu, N. Xiong, Y. Yao, X.Q. Li, S.Z. Wei, Int. J. Refract. Met. Hard Mater. 109 (2022) 105983.

[46] H. Kurishita, M. Asayama, O. Tokunaga, H. Yoshinaga, Mater. Trans., JIM 30 (1989) 1009–1015.
[47] J. Fan, Z. Qian, H. Cheng, J. Tian, C. Cheng, Rare Met. Mater. Eng. 42 (2013) 853–856.
[48] D. Lang, C. Pöhl, D. Holec, J. Schatte, E. Povoden Karadeniz, W. Knabl, H. Clemens, S. Primig, J. Alloy. Compd. 654 (2016) 445–454.
[49] L. Wang, G. Liu, J. Sun, Mater. Res. Express. 4 (2017) 116515.
[50] L.R. Dong, J.H. Li, J.S. Wang, C.H. Wang, J. Zhang, L.Y. Xiao, K.J. Luo, Powder Technol. 346 (2019) 78–84.
[51] X. Chen, B. Li, T. Wang, R. Li, J. Wang, S. Ren, G.J. Zhang, Vacuum 152 (2018) 70–77.
[52] G.J. Zhang, Y.J. Sun, C. Zuo, J.F. Wei, J. Sun, Mater. Sci. Eng. A 483-484 (2008) 350–352.
[53] Z. Dong, N. Liu, W.Q. Hu, X.W. Kong, Z.Q. Ma, Y.C. Liu, Mater. Des. 181 (2019) 108080.
[54] X. Lan, Z.B. Li, H. Zhang, G.H. Zhang, Int. J. Refract. Met. Hard Mater. 110 (2023) 106014.
[55] G.J. Zhang, G. Liu, Y.J. Sun, F. Jiang, L. Wang, R.H. Wang, J. Sun, Int. J. Refract. Met. Hard Mater. 27 (2009) 173–176.
[56] G.J. Zhang, Q. Dang, H. Kou, R.H. Wang, G. Liu, J. Sun, J. Alloy. Compd. 577 (2013) S493–S498.
[57] A.J. Mueller, R. Bianco, R.W. Buckman, Int. J. Refract. Met. Hard Mater. 18 (2000) 205–211.
[58] Y. Wang, D.Z. Wang, H.Y. Liu, W. Zhu, X.Q. Zan, Mater. Sci. Eng. A 558 (2012) 497–501.
[59] W.H. Li, G.J. Zhang, S.X. Wang, B. Li, J. Sun, J. Alloy. Compd. 642 (2015) 34–39.
[60] W.H. Li, T.T. Ai, H.F. Dong, G.J. Zhang, Materials (Basel) 12 (2019) 1–13.
[61] F.A. Mirza, K. Wang, S.D. Bhole, J. Friedman, D.L. Chen, D.R. Ni, B.L. Xiao, Z.Y. Ma, Mater. Sci. Eng. A 661 (2016) 115–125.
[62] T.L. Sun, L.J. Xu, S.Z. Wei, F.N. Xiao, Z. Li, X.M. Fan, Y.C. Zhou, Int. J. Refract. Met. Hard Mater. 86 (2020) 105085.
[63] X.Q. Yang, H. Tan, N. Lin, Z.X. Li, Y.H. He, Int. J. Refract. Met. Hard Mater. 51 (2015) 301–308.
[64] W.Q. Hu, L. Wang, Z.Q. Ma, L.M. Yu, Y.C. Liu, Mater. Sci. Eng. A 818 (2021) 141448.
[65] L. Wang, J. Sun, G. Liu, Y.J. Sun, G.J. Zhang, Int. J. Refract. Met. Hard Mater. 29 (2011) 522–527.
[66] B.V. Cockeram, Metall. Mater. Trans. A 40 (2009) 2843–2860.
[67] J.S. Wang, W. Liu, Z.Y. Ren, F. Yang, Y.M. Wang, Y.h. Du, M.L. Zhou, Curr. Appl. Phys. 11 (2011) 667–672.
[68] G. Liu, G.J. Zhang, F. Jiang, X.D. Ding, Y.J. Sun, J. Sun, E. Ma, Nat. Materr. 12 (2013) 344–350.
[69] S. Vervynckt, K. Verbeken, P. Thibaux, Y. Houbaert, Mater. Sci. Eng. A 528 (2011) 5519–5528.
[70] S. Christian, D.K. Reza, S. Ingo, Acta Mater. 106 (2016) 59–65.
[71] W.Q. Hu, Z. Dong, L.M. Yu, Z.Q. Ma, Y.C. Liu, J. Mater. Sci. Technol. 36 (2020) 84–90.
[72] D.J. Jiang, Z. Dong, Z.F. Du, Q. Zhao, H. Wang, Z.Q. Ma, Mater. Sci. Eng. A 831 (2022) 142344.
[73] G. Gottstein, L.S. Shvindlerman, Acta Mater. 41 (1993) 3267–3275.
[74] S.K. Makineni, A.R. Kini, E.A. Jägle, H. Springer, D. Raabe, B. Gault, Acta Mater. 151 (2018) 31–40.
[75] B.L. Hu, K.S. Wang, P. Hu, S.L. Li, J. Deng, Y.G. Zuo, H.R. Xing, P.F. Feng, V. Paley, A.A. Volinsky, Mater. Sci. Eng. A 759 (2019) 167–171.
[76] R. Li, X. Chen, B. Li, J. Wang, T. Wang, F.X. Yan, G.J. Zhang, Int. J. Refract. Met. Hard Mater. 94 (2021) 105374.
[77] C. Chen, W. Tan, M.P. Wang, Z. Li, Q. Lei, F.Z. Xia, Mater. Sci. Eng. A 527 (2010) 600–605.
[78] P.M. Cheng, S.L. Li, G.J. Zhang, J.Y. Zhang, G. Liu, J.Z. Sun, Mater. Sci. Eng. A 619 (2014) 345–353.
[79] B.V. Cockeram, Mater. Sci. Eng. A 528 (2010) 288–308.
[80] P.Q. Chen, Y.X. Tai, J.G. Cheng, Powder Metall. Technol. 39 (2021) 203–208.
[81] L.B. Chen, R. Wei, K. Tang, G.J. Zhang, F. Jiang, J. Sun, Mater. Trans. 59 (2018) 764–770.
[82] K.S. Wang, J.F. Tan, P. Hu, Z.T. Yu, F. Yang, B.L. Hu, R. Song, H.C. He, A.A. Volinsky, Mater. Sci. Eng. A 636 (2015) 415–420.
[83] G.J. Zhang, Y. Zha, B. Li, W. He, J. Sun, Int. J. Refract. Met. Hard Mater. 41 (2013) 585–589.
[84] H.A. Zhang, D.Z. Wang, S.P. Chen, X.Y. Liu, Mater. Sci. Eng. A 345 (2003) 118–121.
[85] B.L. Hu, J.Y. Han, S.W. Ge, X.J. Hua, S.L. Li, H.R. Xing, K.S. Wang, P. Hu, J.B. Fu, W. Zhang, A.A. Volinsky, E.S. Marchenko, Mater. Sci. Eng. A 831 (2022) 142271.
[86] X.H. Lin, B. Li, L.P. Li, J. Liang, X.Q. Gao, X. Zhang, Rare Metal. 38 (2019) 848–854.
[87] W.H. Li, G.J. Zhang, T.T. Ai, B. Li, R. Li, Mater. Res. Express. 6 (2019) 096593.
[88] W.D.C. Jr, D.G. Rethwisch, Materials Science and Engineering: An Introduction, 10th Edition, Materials Science and Engineering, 1966.
[89] J.X. Zhang, L. Lu, M.L. Zhou, Y.C. Hu, T.Y. Zuo, Int. J. Refract. Met. Hard. Mater. 17 (1999) 405–409.
[90] R. Li, B. Li, X. Chen, J. Wang, F.X. Yan, T. Wang, S. Ren, G.J. Zhang, Mater. Sci. Eng. A 772 (2020) 138684.
[91] W.J. Choi, S.Y. Lee, C.W. Park, J.H. Park, J.M. Byun, Y.D. Kim, Int. J. Refract. Met. Hard Mater. 80 (2019) 238–242.
[92] I. Rosales, J.H. Schneibel, Intermetallics 8 (2000) 885–889.
[93] A.F. Bower, M. Ortiz, J. Mech. Phys. Solids. 39 (1991) 815–858.
[94] P. Ramasundaram, R. Bowman, W. Soboyejo, Mater. Sci. Eng. A 248 (1998) 132–146.
[95] H. Choe, J.H. Schneibel, R.O. Ritchie, Metall. Mater. Trans. A 34 (2003) 225–239.
[96] R. Li, X. Chen, B. Li, J. Wang, T. Wang, F. Yan, G. Zhang, Int. J. Refract. Met. Hard Mater. 94 (2021) 105374.
[97] P.M. Cheng, Z.J. Zhang, G.J. Zhang, J.Y. Zhang, K. Wu, G. Liu, W. Fu, J. Sun, Mater. Sci. Eng. A 707 (2017) 295–305.
[98] F. Ellyin, Fatigue Damage, Crack Growth and Life Prediction, 1997, p. 415.
[99] P. Hu, F. Yang, J. Deng, T. Chang, B.L. Hu, J.F. Tan, K.S. Wang, W.C. Cao, P.F. Feng, H.L. Yu, J. Alloy. Compd. 711 (2017) 64–70.
[100] P. Hu, Y.H. Zhou, T. Chang, Z.T. Yu, K.S. Wang, F. Yang, B.L. Hu, W.C. Cao, H.L. Yu, Mater. Sci. Eng. A 687 (2017) 276–280.
[101] J.L. Ma, W.H. Li, G.X. Wang, Y.Q. Li, H.B. Guo, Z.L. Zhao, W. Li, J. Mater. Eng. Perform. 26 (2017) 4847–4854.
[102] L.J. Xu, S.Z. Wei, Q. Liu, G.S. Zhang, J.W. Li, Tribol. Trans. 56 (2013) 833–840.
[103] R. Li, X. Chen, J. Wang, B. Li, F. Yan, G. Zhang, Int. J. Refract. Met. Hard Mater. 112 (2023) 106167.
[104] P.M. Cheng, G.J. Zhang, J.Y. Zhang, G. Liu, J. Sun, Mater. Sci. Eng. A 640 (2015) 320–329.
[105] S.E. Urreta, F. Louchet, A. Ghilarducci, Mater. Sci. Eng. A 302 (2001) 300–307.
[106] G. Liu, J. Sun, C.W. Nan, K.H. Chen, Acta Mater. 53 (2005) 3459–3468.
[107] P.M. Cheng, C. Yang, P. Zhang, J.Y. Zhang, H. Wang, J. Kuang, G. Liu, J. Sun, J. Mater. Sci. Technol. 130 (2022) 53–63.
[108] E. Arzt, D.S. Wilkinson, Acta Metall. 34 (1986) 1893–1898.
[109] R. Arrabal, A. Pardo, M.C. Merino, M. Mohedano, P. Casajús, K. Paucar, G. Garcés, Corros. Sci. 55 (2012) 301–312.
[110] X.X. Wang, Y.M. Gao, K. Li, J.B. Yan, Y.F. Li, J.B. Feng, Corros. Sci. 69 (2013) 369–375.
[111] W. Cairang, T.S. Li, D.Z. Xue, H.J. Yang, P.M. Cheng, C. Chen, Y.J. Sun, Y. Zeng, X.D. Ding, J. Sun, Corros. Sci. 186 (2021) 109469.
[112] B.A. Pint, Oxid. Met. 45 (1996) 1–37.
[113] R.J. Christensen, V.K. Tolpygo, D.R. Clarke, Acta Mater. 45 (1997) 1761–1766.
[114] S. Majumdar, S. Burk, D. Schliephake, M. Krüger, H.J. Christ, M. Heilmaier, Oxid. Met. 80 (2013) 219–230.
[115] G.J. Zhang, H. Kou, Q. Dang, G. Liu, J. Sun, Int. J. Refract. Met. Hard Mater. 30 (2012) 6–11.
[116] Z. Dong, W.Q. Hu, Z.Q. Ma, C. Li, Y.C. Liu, Mater. Chem. Front. 3 (2019) 1952–1972.
[117] W.Q. Hu, Q.S. Ma, Z.Q. Ma, Y. Huang, Z.M. Wang, Y.C. Liu, Tungsten 1 (2019) 220–228.
[118] J.S. Wang, W. Liu, H.Y. Li, F. Gao, Z.Y. Ren, M.L. Zhou, Trans. Nonferrous Met. Soc. China 20 (2010) 233–237.
[119] W.Q. Hu, Z. Dong, Z.Q. Ma, Y.C. Liu, J. Alloy. Compd. 821 (2020) 153461.
[120] E. Bermejo, T. Dantas, C. Lacour, M. Quarton, Mater. Res. Bull. 30 (1995) 645–652.
[121] Z. Dong, N. Liu, Z.Q. Ma, C.X. Liu, Q.Y. Guo, Y. Yamauchi, H.R. Alamri, Z.A. Alothman, M. Shahriar, A. Hossain, Y.C. Liu, Int. J. Refract. Met. Hard Mater. 69 (2017) 266–272.
[122] M. Xia, Q.Z. Yan, L. Xu, H.Y. Guo, L.X. Zhu, C.C. Ge, J. Nucl. Mater. 434 (2013) 85–89.
[123] T. Ryu, K.S. Hwang, Y.J. Choi, H.Y. Sohn, Int. J. Refract. Met. Hard Mater. 27 (2009) 701–704.
[124] W.Q. Hu, Z. Dong, Z.Q. Ma, Y.C. Liu, Inorg. Chem. Front. 7 (2020) 659–666.
[125] B.H. He, H.L. Yang, J.M. Ruang, Mater. Sci. Eng. Powder Metall. 17 (2012) 234–239.
[126] C.X. Liu, K.S. Wang, P.F. Feng, G. An, Q.L. Yang, H. Zhao, Rare Metal. 33 (2014) 58–64.
[127] G.K. Behera, A. Patra, J. Mater. Eng. Perform. 30 (2021) 6049-6049.
[128] L. Zhang, S. Ukai, T. Hoshino, S. Hayashi, X.H. Qu, Acta Mater. 57 (2009) 3671–3682.
[129] W.Q. Hu, Z. Dong, H. Wang, T. Ahamad, Z.Q. Ma, Int. J. Refract. Met. Hard Mater. 95 (2021) 105453.
[130] W.Q. Hu, T. Sun, C.X. Liu, L.M. Yu, T. Ahamad, Z.Q. Ma, J. Mater. Sci. Technol. 88 (2021) 36–44.
[131] L.Y. Yao, Y.M. Gao, Y.J. Huang, Y.F. Li, X.Y. Huang, P. Xiao, Int. J. Refract. Met. Hard Mater. 98 (2021) 105558.
[132] B.L. Bramfitt, Mater. Trans. 1 (1970) 1987–1995.
[133] R. Ohser Wiedemann, U. Martin, H.J. Seifert, A. Müller, Int. J. Refract. Met. Hard Mater. 28 (2010) 550–557.
[134] G. Lee, C. Manière, J. McKittrick, R. Doerner, D. Nishijima, A. Gattuso, T. Abrams, D. Thomas, C. Back, E.A. Olevsky, J. Nucl. Materr. 516 (2019) 354–359.
[135] Z.Y. Hu, Z.H. Zhang, X.W. Cheng, F.C. Wang, Y.F. Zhang, S.L. Li, Mater. Des. 191 (2020) 108662.
[136] L.Y. Yao, Y.J. Huang, Y.M. Gao, Y.F. Li, X.Y. Huang, Y.R. Wang, Q.K. Liu, C.M. Zhou, Int. J. Refract. Met. Hard Mater. 107 (2022) 105881.
[137] J. Schmelzer, S.K. Rittinghaus, M.B. Wilms, O. Michael, M. Krüger, Int. J. Refract. Met. Hard Mater. 101 (2021) 105623.
[138] L.J. Xu, N. Li, W.L. Song, T.L. Sun, Y.C. Zhou, S.Z. Wei, H.H. Shen, J. Alloy. Compd. 897 (2022) 163110.
[139] A. Lasalmonie, J.L. Strudel, J. Mater. Sci. 21 (1986) 1837–1852.
[140] G.K. Behera, A. Patra, J. Mater. Eng. Perform. 30 (2021) 6039–6048.
[141] Z.P. Guo, L. Wang, C. Wang, Q.L. Li, Coatings 10 (2020) 833.
[142] J.h. Yan, X.F. Zhang, Y. Wang, J.W. Qiu, C.F. Song, J. Mater. Eng. Perform. 32 (2023) 3274–3283.

[143] Z.Z. Wu, N. Zhao, Y. Lu, H.L. Liu, B.H. Duan, X.L. Liu, D.Z. Wang, Trans. Nonferrous Met. Soc. China 32 (2022) 1926–1934.
[144] X.H. Zhang, C.G. Lin, S. Cui, Z.D. Li, Rare Metals 33 (2013) 191–195.
[145] M. Alizadeh, M.M. Aliabadi, J. Alloy. Compd. 509 (2011) 4978–4986.
[146] J.L. Liu, C. Suryanarayana, D. Ghosh, G. Subhash, L.N. An, J. Alloy. Compd. 563 (2013) 165–170.
[147] G.R. Li, H.M. Wang, X.T. Yuan, Y.T. Zhao, Mater. Lett. 99 (2013) 50–53.
[148] M.S. Motta, P.K. Jena, E.A. Brocchi, I.G. Solórzano, Mater. Sci. Eng. C 15 (2001) 175–177.
[149] S. Wei, L. Xu, G. Zhang, J. Li, B. Dai, Appl. Mech. Mater. 120 (2011) 467.
[150] L. Xu, S. Wei, G. Zhang, J. Li, X. Ma, B. Dai, Adv. Mater. Res. 150-151 (2010) 1077–1081.
[151] L.J. Xu, S.Z. Wei, D.D. Zhang, Y. Li, G.S. Zhang, J.W. Li, Int. J. Refract. Met. Hard Mater. 41 (2013) 483–488.
[152] Y.C. Zhou, Y.M. Gao, S.Z. Wei, Y.J. Hu, Rare Metal. 37 (2018) 1046–1054.
[153] L.J. Xu, S.Z. Wei, J.W. Li, G.S. Zhang, B.Z. Dai, Int. J. Refract. Met. Hard Mater. 30 (2012) 208–212.
[154] Y.C. Zhou, Y.M. Gao, S.Z. Wei, K.M. Pan, Y.J. Hu, Int. J. Refract. Met. Hard Mater. 54 (2016) 186–195.
[155] B. Chen, Z.B. Li, G.H. Zhang, K.C. Chou, JOM 73 (2021) 3451–3459.
[156] G.D. Sun, G.H. Zhang, K.C. Chou, J. Mater. Res. Technol. 8 (2019) 5753–5762.
[157] A.M. Tahir, R. Janisch, A. Hartmaier, Modell. Simul. Mater. Sci. Eng. 21 (2013) 075005.
[158] X.M. Fan, L.J. Xu, S.Z. Wei, L.Y. Yao, T.L. Sun, Y.C. Zhou, K.M. Pan, F.N. Xiao, K. Sun, Ceram. Int. 46 (2020) 10400–10408.
[159] G.J. Zhang, Y.J. Sun, R.M. Niu, J.Z. Sun, J.F. Wei, B.H. Zhao, L.X. Yang, Adv. Eng. Mater. 6 (2004) 943–948.
[160] P.M. Cheng, S.L. Li, G.J. Zhang, J.Y. Zhang, G. Liu, J. Sun, Mater. Sci. Eng. A 619 (2014) 345–353.
[161] G. Hinrichsen, Mater. Sci. Technol. (1994).
[162] T.L. Sun, L.J. Xu, S.Z. Wei, K.M. Pan, W.H. Li, Y.C. Zhou, Z.M. Huang, Trans. Nonferrous Met. Soc. China 30 (2020) 3307–3321.
[163] Y.C. Zhou, S.Z. Wei, L.J. Xu, X.Q. Li, J. Alloy. Compd. 769 (2018) 340–346.
[164] Y.C. Zhou, Y.M. Gao, S.Z. Wei, Y.J. Hu, Microsc. Microanal. 22 (2016) 122–130.
[165] B. Meng, M. Wan, X.D. Wu, Y.K. Zhou, C. Chang, Int. J. Refract. Met. Hard Mater. 45 (2014) 41–47.
[166] A. Chaudhuri, A.N. Behera, A. Sarkar, R. Kapoor, R.K. Ray, S. Suwas, Acta Mater. 164 (2019) 153–164.
[167] L.Y. Yao, Y.M. Gao, L.J. Xu, Met. Mater. Int. 27 (2020) 5335–5345.
[168] C.J. Wang, L.Q. Zhang, S.Z. Wei, K.M. Pan, X.C. Wu, Q.K. Li, Mater. Sci. Eng. A 744 (2018) 79–85.
[169] Y.C. Zhou, S.Z. Wei, L.M. Wang, L.J. Xu, X.Q. Li, K.M. Pan, J. Alloy. Compd. 823 (2020) 153748.
[170] A. Chaudhuri, A. Sarkar, S. Suwas, Int. J. Refract. Met. Hard Mater. 73 (2018) 168–182.
[171] C.P. Cui, X.W. Zhu, Adv. Process. Metall. 73 (2021) 1646–1651.
[172] J.A.M. Van Liempt, Nature 115 (1925) 194-194.
[173] Y. Kim, K.H. Lee, E.P. Kim, D.I. Cheong, S.H. Hong, Int. J. Refract. Met. Hard Mater. 27 (2009) 842–846.
[174] Z. Dong, Z.Q. Ma, Y.C. Liu, Acta Mater. 220 (2021) 117309.
[175] C.P. Cui, Y.M. Gao, S.Z. Wei, G.S. Zhang, Y.C. Zhou, X.W. Zhu, S.L. Guo, Appl. Phys. A 122 (2016) 214.
[176] O. Lenchuk, J. Rohrer, K. Albe, Acta Mater. 135 (2017) 150–157.
[177] C.P. Cui, Y.M. Gao, S.Z. Wei, G.S. Zhang, X.W. Zhu, S.L. Guo, High Temp. Mater. Process. 36 (2017) 163–166.
[178] C.P. Cui, X.W. Zhu, Q. Li, M. Zhang, G.P. Zhu, High Temp. Mater. Process. 39 (2020) 595–598.
[179] R. Li, B. Li, T. Wang, S. Ren, X. Chen, J. Wang, G. Zhang, J. Alloy. Compd. 743 (2018) 716–727.
[180] Z. Dong, S.H. Chen, S.C. Liu, Z.Q. Ma, L.M. Yu, J. Alloy. Compd. 903 (2022) 163982.
[181] C.P. Cui, X.W. Zhu, S.L. Liu, Q. Li, M. Zhang, G.P. Zhu, S.Z. Wei, J. Alloy. Compd. 768 (2018) 81–87.
[182] L.J. Xu, T.L. Sun, Y.C. Zhou, F.N. Xiao, M.J. Zhang, S.Z. Wei, J. Alloy. Compd. 860 (2021) 158289.
[183] M.L. Xiao, F.G. Li, H.F. Xie, Y.F. Wang, Mater. Des. 34 (2012) 112–119.
[184] C.P. Cui, Y.M. Gao, S.Z. Wei, G.S. Zhang, Y.C. Zhou, X.W. Zhu, J. Alloy. Compd. 716 (2017) 321–329.
[185] E.Z. Silva, H. Kestler, H.R.Z. Sandim, Int. J. Refract. Met. Hard Mater. 73 (2018) 74–78.
[186] L.Y. Yao, S.Z. Wei, Y.C. Zhou, L.J. Xu, C. Chen, T.L. Sun, P.P. Shi, Int. J. Refract. Met. Hard Mater. 75 (2018) 202–210.
[187] C.P. Cui, X.W. Zhu, S.L. Liu, Q. Li, J. Alloy. Compd. 752 (2018) 308–316.
[188] C.P. Cui, X.W. Zhu, Q. Li, M. Zhang, G.P. Zhu, S.L. Liu, J. Alloy. Compd. 829 (2020) 154630.
[189] H.J. Shi, C. Korn, G. Pluvinage, Mater. Sci. Eng. A 247 (1998) 180–186.
[190] H.J. Shi, L.S. Niu, C. Korn, G. Pluvinage, J. Nucl. Mater. 278 (2000) 328–333.
[191] W.L. Song, L.J. Xu, N. Li, Y.C. Zhou, T.L. Sun, Z. Li, H.H. Shen, S.Z. Wei, J. Alloy. Compd. 867 (2021) 159118.
[192] Z.N. Xu, L.J. Xu, W.L. Song, Y.C. Zhao, Y.C. Zhou, W. Liu, L. Yang, S.Z. Wei, Vacuum 203 (2022) 111170.
[193] L.L. Yang, Q.F. Zhang, Z.Y. He, X.G. Li, Int. J. Refract. Met. Hard Mater. 67 (2017) 56–67.
[194] X.Y. Ding, L.M. Luo, H.Y. Chen, G.N. Luo, X.Y. Zhu, X. Zan, J.G. Cheng, Y.C. Wu, Fusion Eng. Des. 92 (2015) 29–34.
[195] L.M. Luo, X.Y. Tan, H.Y. Chen, G.N. Luo, X.Y. Zhu, J.G. Cheng, Y.C. Wu, Powder Technol. 273 (2015) 8–12.
[196] W.Q. Hu, X.W. Kong, Z.F. Du, A. Khan, Z.Q. Ma, J. Alloy. Compd. 859 (2021) 157774.
[197] W.Q. Hu, Z.F. Du, Z.Z. Dong, L.M. Yu, T. Ahamad, Z.Q. Ma, Scr. Mater. 198 (2021) 113831.
[198] R. Ohser Wiedemann, C. Weck, U. Martin, A. Müller, H.J. Seifert, Int. J. Refract. Met. Hard Mater. 32 (2012) 1–6.
[199] C. Tuzemen, B. Yavas, I. Akin, O. Yucel, F. Sahin, G. Goller, J. Alloy. Compd. 781 (2019) 433–439.
[200] W.W. Zhou, X.H. Sun, K. Kikuchi, N. Nomura, K. Yoshimi, A. Kawasaki, Mater. Des. 146 (2018) 116–124.
[201] S. Miyamoto, K. Yoshimi, S.H. Ha, T. Kaneko, J. Nakamura, T. Sato, K. Maruyama, R. Tu, T. Goto, Metall. Mater. Trans. A 45 (2014) 1112–1123.
[202] S.Y. Kamata, D. Kanekon, Y. Lu, N. Sekido, K. Maruyama, G. Eggeler, K. Yoshimi, Sci. Rep. 8 (2018) 10487.
[203] M.Le Flem, A. Allemand, S. Urvoy, D. Cédat, C. Rey, J. Nucl. Mater. 380 (2008) 85–92.
[204] Y. Hiraoka, Int. J. Refract. Met. Hard Mater. 21 (2003) 265–270.
[205] K. Yoshimi, J. Nakamura, D. Kanekon, S. Yamamoto, K. Maruyama, H. Katsui, T. Goto, JOM 66 (2014) 1930–1938.
[206] P.N. Browning, J. Fignar, A. Kulkarni, J. Singh, Int. J. Refract. Met. Hard Mater. 62 (2017) 78–84.
[207] J. Zhao, L.C. Liu, H.R. Gong, X. Gong, Surf. Coat. Technol. 382 (2020) 125158.
[208] T. Takida, M. Mabuchi, M. Nakamura, T. Igarashi, Y. Doi, N. Takekazu, Mater. Sci. Eng. A 276 (2000) 269–272.
[209] B.L. Hu, K.S. Wang, P. Hu, Y.T. Su, S.L. Li, H.R. Xing, J.Y. Han, S.W. Ge, X.J. Hua, J.B. Fu, T. Chang, Int. J. Refract. Met. Hard Mater. 92 (2020) 105336.
[210] K. Jing, R. Liu, Z.M. Xie, J.G. Ke, X.P. Wang, Q.F. Fang, C.S. Liu, H. Wang, G. Li, X.B. Wu, Acta Mater. 227 (2022) 117725.
[211] K. Jing, X. Cheng, R. Liu, X.F. Xie, Z.M. Xie, X.B. Wu, H. Wang, G. Li, Q.F. Fang, C.S. Liu, X.P. Wang, Mater. Sci. Eng. A 854 (2022) 143803.
[212] H.Si Abdelkader, H.I. Faraoun, C. Esling, J. Appl. Phys. 110 (2011) 044901.
[213] J. Becker, D. Breuer, I. Bogomol, M. Krüger, Crystals 12 (2022) 1534.
[214] S. Nakayama, N. Sekido, S. Uemura, S. Tsurekawa, K. Yoshimi, Mater. Trans. 59 (2018) 518–527.
[215] J.N. Gan, Q.M. Gong, Y.Q. Jiang, H. Chen, Y.L. Huang, K. Du, Y.Y. Li, M. Zhao, F. Lin, D.M. Zhuang, J. Alloy. Compd. 796 (2019) 167–175.
[216] Y. Katoh, G. Vasudevamurthy, T. Nozawa, L.L. Snead, J. Nucl. Mater. 441 (2013) 718–742.